REPORT DOCUMENTATION PAGE

Form Approved
OMB NO. 0704-0188

1. AGENCY USE ONLY (Leave Blank)	2. REPORT DATE	3. REPORT TYPE AND DATES COVERED
	December 18, 2000	FINAL 01 Jun 96 – 31 May 01

4. TITLE AND SUBTITLE
Design, Analysis and Processing of Functionally Graded Structural Materials - Final Report

5. FUNDING NUMBERS
DAAH04-96-1-0197

6. AUTHOR(S)
R.J. Diefendorf, J. G. Goree, M. Grujicic, P.F. Joseph

7. PERFORMING ORGANIZATION NAME(S) AND ADDRESS(ES)
Clemson University, Clemson, SC 29634

8. PERFORMING ORGANIZATION REPORT NUMBER
6473 - II

9. SPONSORING / MONITORING AGENCY NAME(S) AND ADDRESS(ES)
U. S. Army Research Office
P.O. Box 12211
Research Triangle Park, NC 27709-2211

10. SPONSORING / MONITORING AGENCY REPORT NUMBER
ARO 35814.26-MS-DPS

11. SUPPLEMENTARY NOTES
The views, opinions and/or findings contained in this report are those of the author(s) and should not be construed as an official Department of the Army position, policy or decision, unless so designated by the documentation.

12 a. DISTRIBUTION / AVAILABILITY STATEMENT	12 b. DISTRIBUTION CODE
Approved for public release; distribution unlimited.	

13. ABSTRACT (Maximum 200 words)

A multi-length scale computational methodology is developed to analyze processing/microstructure and microstructure/properties/performance relationship in advanced structural materials. Such methodology is based on combining scientific and engineering disciplines of fluid mechanics, heat transfer, chemical gas/surface thermodynamics and kinetics, atomistic modeling techniques, stochastic microstructure evolution simulation methods, nonlinear fracture and singular stress analysis, and micro-mechanics analytical and computational approaches. This methodology is then applied to advanced coating and functionally graded materials processed by the chemical vapor deposition (CVD) and the Laser Engineered Net Shaping (LENS™) processes. The methodology allows the establishment of direct links between process parameters (temperature, pressure, flow rates, laser rastering velocity, etc.), the resulting materials microstructure (grain size and distribution, morphological and crystallographic texture, etc.) and properties (strength, strain-to-fracture, etc.). In response to the computational challenges of multi-length scale modeling, parallel computing is utilized and a highly-efficient inter-processor communications method is developed which substantially reduces the simulation time.

14. SUBJECT TERMS	15. NUMBER OF PAGES
Functionally Graded Materials, Atomistic Simulation, Decohesion, Voronoi Cell FEM, nonlinear fracture, mixed mode fracture, multiple asymptotic crack solutions, Chemical Vapor Deposition, Monte Carlo, Crystal Plasticity, Computational Fluid Dynamics	50
	16. PRICE CODE

17. SECURITY CLASSIFICATION OR REPORT	18. SECURITY CLASSIFICATION ON THIS PAGE	19. SECURITY CLASSIFICATION OF ABSTRACT	20. LIMITATION OF ABSTRACT
UNCLASSIFIED	UNCLASSIFIED	UNCLASSIFIED	UL

NSN 7540-01-280-5500

Standard Form 298 (Rev.2-89)
Prescribed by ANSI Std. 239-18

Table of Contents

List of Appendices

Statement of the Problem Studied

Advanced structural materials are generally developed using various empirical methods. Such methods are typically time-consuming and costly and do not enable the advances in development of one type of material to be easily utilized to make similar advances in development of materials of other types. The main objective of the present work was to develop a multi-length scale methodology for analyzing the relationships between: (a) process parameters and the resulting materials microstructure and (b) microstructure properties and performance in advanced materials (coatings, functionally-graded materials, etc.) processed by CVD and LENS™ techniques. The work was also aimed at combining various scientific and engineering disciplines such as: chemical thermodynamics and kinetics, fluid dynamics and heat transfer, stochastic computational methods for prediction of microstructural evolution, atomistic simulation techniques, micromechanics approaches and nonlinear fracture mechanics.

Summary of Most Important Results

1. Atomic simulations combined with the first-principle electronic-structure calculation-based interatomic potentials, have been utilized to determine the grain boundary/interface decohesion potentials and relate them to the interface orientation and grains misorientation. This approach revealed a critical role of grain boundary sliding in the process of decohesion. This work was done in collaboration with Dr. Genrich L. Krasko of the U.S. Army Research Laboratory in Aberdeen Proving Ground, and has resulted in eight journal publications [1-8] and one technical report [9]. Selected results pertaining to this portion of the project are given in Appendix A.

2. The Voronoi Cell Finite Element formulation has been utilized to determine the effective microstructure-sensitive elastic and plastic properties of functionally graded materials. Results show that the effective properties of FGMs are more reliably determined using this method than the more commonly used self-consistent approach. This portion of the work has resulted in two journal publications [10,11]. Selected results pertaining to this portion of the project are given in Appendix B.

3. A combined finite element, singular value decomposition method has been established to study the asymptotic singular stress fields, including higher order terms, for cracks, interface cracks and wedges in power law hardening materials. This method is versatile with respect to geometry and loading. These capabilities have led to the following two key findings for fracture in functionally graded materials: 1) For plane strain fracture near conditions of pure mode I, the asymptotic stress field is not mixed mode. Rather it is in a higher order form. In FGMs, due to the combination of materials, it is likely that a crack will grow in a manner that fluctuates around pure symmetric mode I conditions, where this new asymptotic solution is required. 2) For interface fracture it has been discovered that two asymptotic solutions are necessary to describe the full range of loading conditions. The first is a higher order solution, again near mode I, and the second is believed to be non-separable. Efforts to determine this non-separable solution are underway. This portion of the work resulted in five journal publications [12-16] with one in review [17], another about to be submitted [18] and two presentations [19,20]. Selected results pertaining to this portion of the project are given in Appendix C.

4. Multi-length scale modeling of the chemical vapor deposition process is carried out to combine the reactor scale, the grain-size scale and the atomistic scale. This modeling effort combines various approaches from the disciplines of reactive-gas fluid dynamics and heat transfer, gas and surface chemical thermodynamics and kinetics, van-der Drift-type modeling of microstructure evolution and kinetic Monte Carlo atomistic-scale deposition modeling techniques. The approach allows determination of the relationship between the process parameter and the microstructure and quality of the CVD-grown film/coating. This portion of the work has resulted in five journal publications [21-25] and one conference presentation [26]. Selected results pertaining to this portion of the project are given in Appendix D.

5. To develop experimental capabilities needed to complement the work described above, a large-scale CVD reactor has been installed at Clemson University. This equipment is valued at approximately $500,000, and was donated by Dupont to the P.I., who was instrumental in the design of the equipment. Preliminary runs involving CVD of TiN coatings have been carried out and the results obtained indicate that major redesign of the CVD reactor is needed in order to enable the level of process control suggested by the multi-length scale simulation studies after CVD process. Selected pictures showing the CVD reactor are given in Appendix E.

6. A large-scale parallel-computing Monte Carlo Model is developed to analyze microstructure evolution during LENS™ rapid manufacturing process. The model enables establishment of the relationship between the process parameters and the resulting materials microstructure. This portion of the work has resulted in one manuscript, which will be submitted for publication in January 2001 [27].

List of All Publications and Technical Reports

Journal Publications

1. Grujicic, M., Zhao, H. and Krasko, G.L., "Atomistic Simulation of S3 (111) Grain Boundary Fracture in Tungsten Containing Various Impurities," International Journal of Refractory Metals and Hard Materials, Vol. 15, 1997, pp. 341-355.

2. Joseph, P.F. and Zhang, N., "Multiple Root Solutions, Wedge Paradoxes, and Singular Stress States that are not Variable-Separable," Composites Science and Technology, Vol. 58, 1998, pp. 1839-1859.

3. Grujicic, M. and Zhao, H., "Optimization of 316 Stainless Steel/Alumina Functionally Graded Materials for Reduction of Damage Induced by Thermal Residual Stresses," Materials Science and Engineering, A252, 1998, pp. 117-132.

4. Grujicic, M. and Zhang, Y. "Determination of Effective Elastic Materials Properties in Functionally Graded Materials Using Voronoi Cell Finite Element Formulation," Materials Science and Engineering, A251, 1998, pp.64-76.

5. Zhang, N. and Joseph, P.F., "A Nonlinear Finite Element Eigenanalysis of Singular Plane Stress Fields in Bi-material Wedges Including Complex Eigenvalues," International Journal of Fracture, Vol. 90, 1999, pp. 175-207.

6. Zhang, N. and Joseph, P.F., "A Nonlinear Finite Element Eigenanalysis of Singular Stress Fields in Bi-material Wedges for Plane Strain," International Journal of Fracture, Vol. 94, 1998, pp. 299-319.

7. Grujicic, M., Zhao, H. and Krasko, G., "Atomistic Simulation of Effect of Impurities on $\Sigma 3$ (111) Grain Boundary Fracture in Tungsten," Journal of Computer-Aided Materials Design, 4, 1997, pp. 183-192.

8. Grujicic, M. and Lai, S., "Effect of Martensitic Transformation in Ti-15 at % V β-phase Particles on Lamellar Boundary Decohesion in γ-TiAl: Part 1 Derivation of Interface Decohesion Potentials," Journal of Materials Science, 33, 1998, pp. 4385-4400.

9. Grujicic, M. and Lai, S., "Effect of Martensitic Transformation in Ti-15 at % V β-phase Particles on Lamellar Boundary Decohesion in γ-TiAl: Part 2 Finite Element Analysis of Crack-Bridging Phenomenon," Journal of Materials Science, 33, 1998, pp. 4401-4415.

10. Grujicic, M., and Lai, S., "Atomistic Simulation of Chemical Vapor Deposition of (111)-oriented Diamond Film Using a Kinetic Monte Carlo Method," Journal of Materials Science, 34, 1999, pp. 7-20.

11. Grujicic, M., and Zhang, Y., "Crystal Plasticity Analysis of the Effect of Dispersed b-phase on Deformation and Fracture of Lamellar $\gamma + \alpha_2$ Titanium Aluminide," Materials Science and Engineering, A265, 1999, pp. 285-300.

12. Grujicic, M., and Zhang, Y., "Combined Atomistic-Crystal Plasticity Analysis of the Effect of Beta Phase Precipitates on Deformation and Fracture of Lamellar $\gamma + \alpha_2$ Titanium Aluminide," Journal of Materials Science, 34, 1999, pp. 1419-1437.

13. Gadi, K.S., Joseph, P.F., Zhang, N. and Kaya, A.C., "Thermally induced logarithmic singularities in a composite wedge and other anomalies," Engineering Fracture Mechanics, 65, 2000, pp. 645-664.

14. Loghin, A., Zhang, N. and Joseph, P.F., "A Nonlinear Finite Element Eigenanalysis of Antiplane Shear Including Higher Order Terms," Engineering Fracture Mechanics, 66, 2000, pp. 441-454.

15. Grujicic, M., and Zhang, Y., "Crystal Plasticity Analysis of Stress-Assisted Martensitic Transformation in Ti-10V-2Fe-3Al (wt.%)," Journal of Materials Science, 35, 2000, pp. 4635-4647.

16. Grujicic, M., and Lai, S., "Grain-scale Modeling of Microstructure Evolution in CVD-grown Polycrystalline Diamond Films," Journal of Materials Synthesis and Processing, 2000, pp. 73-86.

17. Grujicic, M., and Lai, S., "Multi-length Scale Modeling of CVD of Diamond: Part I A Combined Reactor Scale/Atomic Scale Analysis," Journal of Materials Science, 35, 2000, pp. 5359-5369.

18. Grujicic, M., and Lai, S., "Multi-length Scale Modeling of CVD of Diamond: Part II A Combined Atomic scale/Grain Scale Analysis," Journal of Materials Science, 35, 2000, pp. 5371-5381.

19. Grujicic, M., Zhao, H. and Krasko, G., "Atomistic Simulation of $\Sigma 3$ (111) Grain Boundary in Tungsten Containing Various Impurities," Army Research Laboratory, ARL-TR-2051, September 1999.

20. Grujicic, M. and Lai, S., "Multi-Length Scale Modeling of Chemical Vapor Deposition of Titanium Nitride Coatings,"

21. Grujicic, M and Columbus, D., "A Comparative Discrete-Dislocation/Crystal-Plasticity Analysis of Bending of a Single Crystalline Microbeam," accepted for publication in Journal of Materials Science, November 2000.

22. Miller, R.S., Cao, G, and Grujicic, M., "Monte Carlo Simulation of Three-Dimensional Non-isothermal Microstructure Evolution: Application to LENS^{TM} Rapid Fabrication," to

be submitted for publication in Journal of Materials Synthesis and Processing, January 2001

23. Loghin, A. and Joseph, P.F., "Loading Dependent Higher Order Asymptotic Solutions in Nonlinear Mixed Mode Fracture," submitted to Engineering Fracture Mechanics, October 2000.

Conference Presentations

1. Joseph, P.F. and Erdogan, F, "Stress Field Near the Tip of a Crack Parallel to an Interface," 13th Congress of Applied Mechanics, University of Florida, June, 1998.

2. K.S. Gadi, Joseph, P.F., B. Han, N. Zhang, and A.C. Kaya, "Thermally Induced Logarithmic Stress Singularities in a Composite Wedge," ASME IMECE, Anaheim, CA, November 1998.

3. Grujicic, M., Diefendorf, R.S. and Lai, S.G., "Multi-length scale Modeling of CVD of Diamond," International Conference on Carbon, Charleston, S.C., July 11-15, 1999.

4. Loghin, A. and Joseph, P.F., "A Nonlinear Finite Element Analysis for Higher Order Terms," 37th meeting of the Society of Engineering Science, Columbia, SC, October 23-35, 2000.

List of All Participating Scientific Personnel Showing Any Advanced Degrees Earned by Them While Employed on the Project

Prof. R. Judd Diefendorf	P.I.
Prof. James. G. Goree	Co-P.I.
Prof. Mica Grujicic	Co-P.I.
Prof. Paul F. Joseph	Co-P.I.
Mr. Ningsheng Zhang	Received PhD degree in December 1997
Mr. Shugang Lai	Received PhD degree in May 2000
Mr. Hezeng Li	Received MS degree in December 1999
Mr. Hui Zhao	PhD candidate. Did not pass PhD qualifying exam. Left the University January 1999.
Mr. Yun Zhang	PhD candidate. Did not pass PhD qualifying exam. Left the University August 1999.
Mr. Michael Brown	MS candidate. Transferred to Business School January 2000.
Mr. Derek Columbus	MS candidate. To graduate in January 2001
Mr. Guoxin Cao	PhD degree. Started in August 2000
Mr. Adrian Loghin	PhD candidate. To receive diploma in May 2001.

Bibliography

1. Grujicic, M., Zhao, H. and Krasko, G.L., "Atomistic Simulation of S3 (111) Grain Boundary Fracture in Tungsten Containing Various Impurities," International Journal of Refractory Metals and Hard Materials, Vol. 15, 1997, pp. 341-355.

2. Grujicic, M., Zhao, H. and Krasko, G., "Atomistic Simulation of Effect of Impurities on Σ3 (111) Grain Boundary Fracture in Tungsten," Journal of Computer-Aided Materials Design, 4, 1997, pp. 183-192.

3. Grujicic, M. and Lai, S., "Effect of Martensitic Transformation in Ti-15 at % V β-phase Particles on Lamellar Boundary Decohesion in γ-TiAl: Part 1 Derivation of Interface Decohesion Potentials," Journal of Materials Science, 33, 1998, pp. 4385-4400.

4. Grujicic, M. and Lai, S., "Effect of Martensitic Transformation in Ti-15 at % V β-phase Particles on Lamellar Boundary Decohesion in γ-TiAl: Part 2 Finite Element Analysis of Crack-Bridging Phenomenon," Journal of Materials Science, 33, 1998, pp. 4401-4415.

5. Grujicic, M., and Zhang, Y., "Crystal Plasticity Analysis of the Effect of Dispersed b-phase on Deformation and Fracture of Lamellar $\gamma + \alpha_2$ Titanium Aluminide," Materials Science and Engineering, A265, 1999, pp. 285-300.

6. Grujicic, M., and Zhang, Y., "Combined Atomistic-Crystal Plasticity Analysis of the Effect of Beta Phase Precipitates on Deformation and Fracture of Lamellar $\gamma + \alpha_2$ Titanium Aluminide," Journal of Materials Science, 34, 1999, pp. 1419-1437.

7. Grujicic, M., and Zhang, Y., "Crystal Plasticity Analysis of Stress-Assisted Martensitic Transformation in Ti-10V-2Fe-3Al (wt.%)," Journal of Materials Science, 35, 2000, pp. 4635-4647.

8. Grujicic, M and Columbus, D., "A Comparative Discrete-Dislocation/Crystal-Plasticity Analysis of Bending of a Single Crystalline Microbeam," accepted for publication in Journal of Materials Science, November 2000.

9. Grujicic, M., Zhao, H. and Krasko, G., "Atomistic Simulation of Σ3 (111) Grain Boundary in Tungsten Containing Various Impurities," Army Research Laboratory, ARL-TR-2051, September 1999.

10. Grujicic, M. and Zhao, H., "Optimization of 316 Stainless Steel/Alumina Functionally Graded Materials for Reduction of Damage Induced by Thermal Residual Stresses," Materials Science and Engineering, A252, 1998, pp. 117-132.

11. Grujicic, M. and Zhang, Y. "Determination of Effective Elastic Materials Properties in Functionally Graded Materials Using Voronoi Cell Finite Element Formulation," Materials Science and Engineering, A251, 1998, pp.64-76.

12. Joseph, P.F. and Zhang, N., "Multiple Root Solutions, Wedge Paradoxes, and Singular Stress States that are not Variable-Separable," Composites Science and Technology, Vol. 58, 1998, pp. 1839-1859.

13. Zhang, N. and Joseph, P.F., "A Nonlinear Finite Element Eigenanalysis of Singular Plane Stress Fields in Bi-material Wedges Including Complex Eigenvalues," International Journal of Fracture, Vol. 90, 1999, pp. 175-207.

14. Zhang, N. and Joseph, P.F., "A Nonlinear Finite Element Eigenanalysis of Singular Stress Fields in Bi-material Wedges for Plane Strain," International Journal of Fracture, Vol. 94, 1998, pp. 299-319.

15. Gadi, K.S., Joseph, P.F., Zhang, N. and Kaya, A.C., "Thermally induced logarithmic singularities in a composite wedge and other anomalies," Engineering Fracture Mechanics, 65, 2000, pp. 645-664.

16. Loghin, A., Zhang, N. and Joseph, P.F., "A Nonlinear Finite Element Eigenanalysis of Antiplane Shear Including Higher Order Terms," Engineering Fracture Mechanics, 66, 2000, pp. 441-454.

17. Loghin, A. and Joseph, P.F., "Loading Dependent Higher Order Asymptotic Solutions in Nonlinear Mixed Mode Fracture," submitted to Engineering Fracture Mechanics, October 2000.

18. Loghin, A., Zhang, N. and Joseph, P.F., "Near Mode I Fracture in Power Law Hardening Materials," to be submitted for publication, January, 2001.

19. K.S. Gadi, Joseph, P.F., B. Han, N. Zhang, and A.C. Kaya, "Thermally Induced Logarithmic Stress Singularities in a Composite Wedge," ASME IMECE, Anaheim, CA, November 1998.

20. Loghin, A. and Joseph, P.F., "A Nonlinear Finite Element Analysis for Higher Order Terms," 37th meeting of the Society of Engineering Science, Columbia, SC, October 23-35, 2000.

21. Grujicic, M., and Lai, S., "Atomistic Simulation of Chemical Vapor Deposition of (111)-oriented Diamond Film Using a Kinetic Monte Carlo Method," Journal of Materials Science, 34, 1999, pp. 7-20.

22. Grujicic, M., and Lai, S., "Grain-scale Modeling of Microstructure Evolution in CVD-grown Polycrystalline Diamond Films," Journal of Materials Synthesis and Processing, 2000, pp., 73-85.

23. Grujicic, M., and Lai, S., "Multi-length Scale Modeling of CVD of Diamond: Part I A Combined Reactor Scale/Atomic Scale Analysis," Journal of Materials Science, 35, 2000, pp. 5359-5369.

24. Grujicic, M., and Lai, S., "Multi-length Scale Modeling of CVD of Diamond: Part II A Combined Atomic scale/Grain Scale Analysis," Journal of Materials Science, 35, 2000, pp. 5371-5381.

25. Grujicic, M. and Lai, S., "Multi-Length Scale Modeling of Chemical Vapor Deposition of Titanium Nitride Coatings," accepted for publication in Journal of Materials Science, November 2000.

26. Grujicic, M., Diefendorf, R.S. and Lai, S.G., "Multi-length scale Modeling of CVD of Diamond," International Conference on Carbon, Charleston, S.C., July 11-15, 1999.

27. Miller, R.S., Cao, G, and Grujicic, M., "Monte Carlo Simulation of Three-dimensional Non-isothermal Microstructure Evolution: Application to LENS^{TM} Rapid Fabrication," to be submitted for publication in Journal of Materials Synthesis and Processing, January 2001

Appendix A

Multi-length Scale Modeling
Of
Microstructure Property Relations

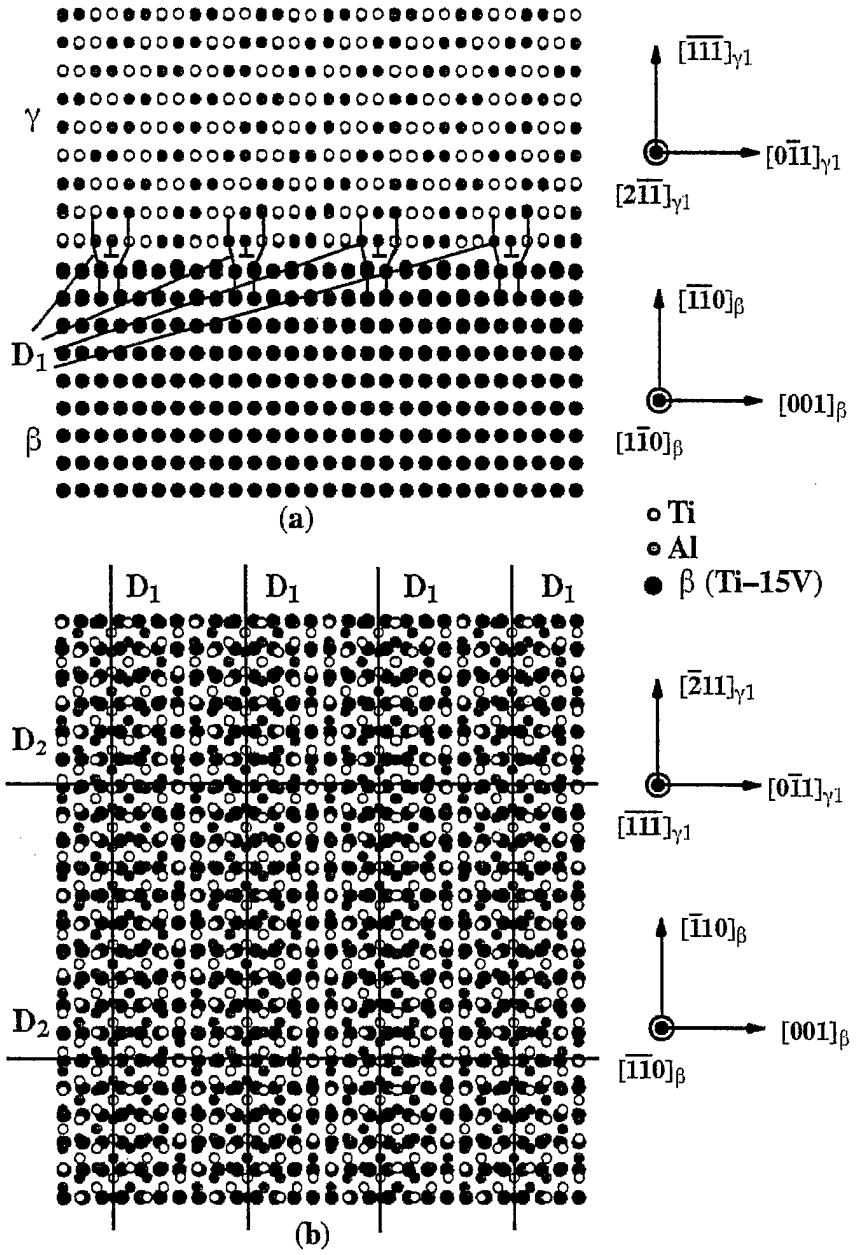

Figure 7 Equilibrium configuration of the $(\bar{1}\bar{1}0)_\beta/(\bar{1}\bar{1}\bar{1})_\gamma$ interface (bicrystal A): (a) Atomic positions projected onto the $(1\bar{1}0)_\beta/(2\bar{1}\bar{1})_\gamma$ plane; (b) Atomic positions projected onto the $(\bar{1}\bar{1}0)_\beta/(\bar{1}\bar{1}\bar{1})_\gamma$ interface plane. Interfacial dislocations are marked as D_1 and D_2.

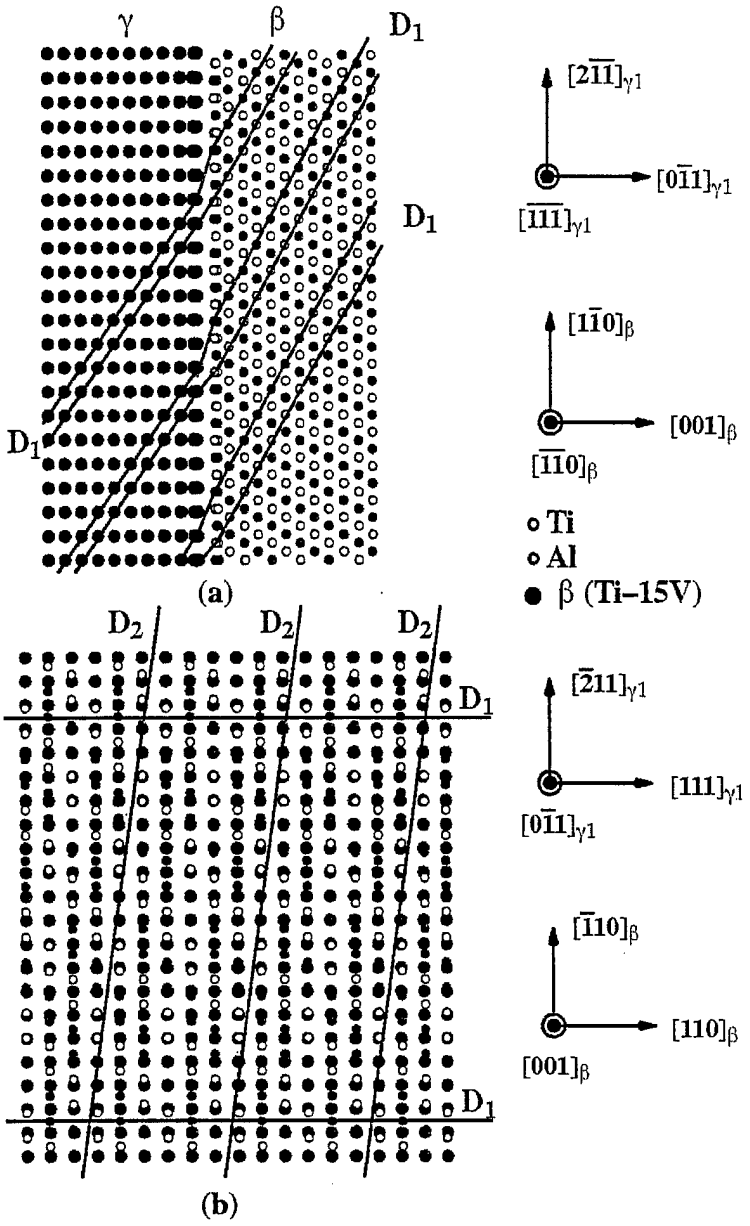

Figure 8 Equilibrium configuration of the $(001)_\beta/(0\bar{1}1)_\gamma$ interface (bicrystal B): (a) Atomic positions projected onto the $(\bar{1}10)_\beta/(\bar{1}\bar{1}\bar{1})_\gamma$ plane; (b) Atomic positions projected onto the $(001)_\beta/(0\bar{1}1)_\gamma$ interface plane. Interfacial dislocations are marked as D_1 and D_2.

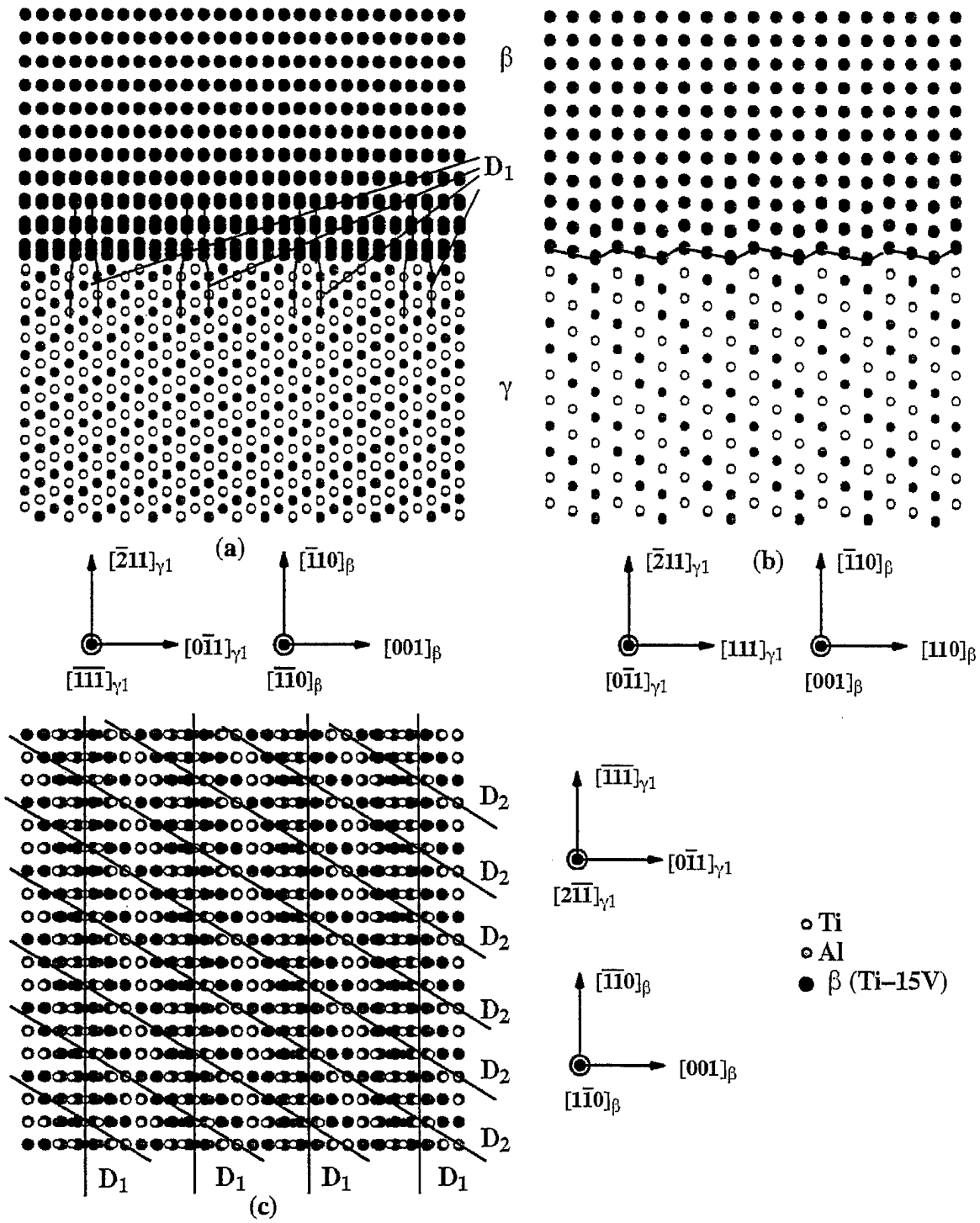

Figure 9 Equilibrium configuration of the $(1\bar{1}0)_\beta/(2\bar{1}\bar{1})_\gamma$ interface (bicrystal C): (a) Atomic positions projected onto the $(\bar{1}10)_\beta/(\bar{1}\bar{1}\bar{1})_\gamma$ plane; (b) Atomic positions projected onto the $(\bar{0}0\bar{1})_\beta/(0\bar{1}\bar{1})_\gamma$ plane; (c) Atomic positions projected onto the $(1\bar{1}0)_\beta/(2\bar{1}\bar{1})_\gamma$ interface plane. Interfacial dislocations are marked as D_1 and D_2.

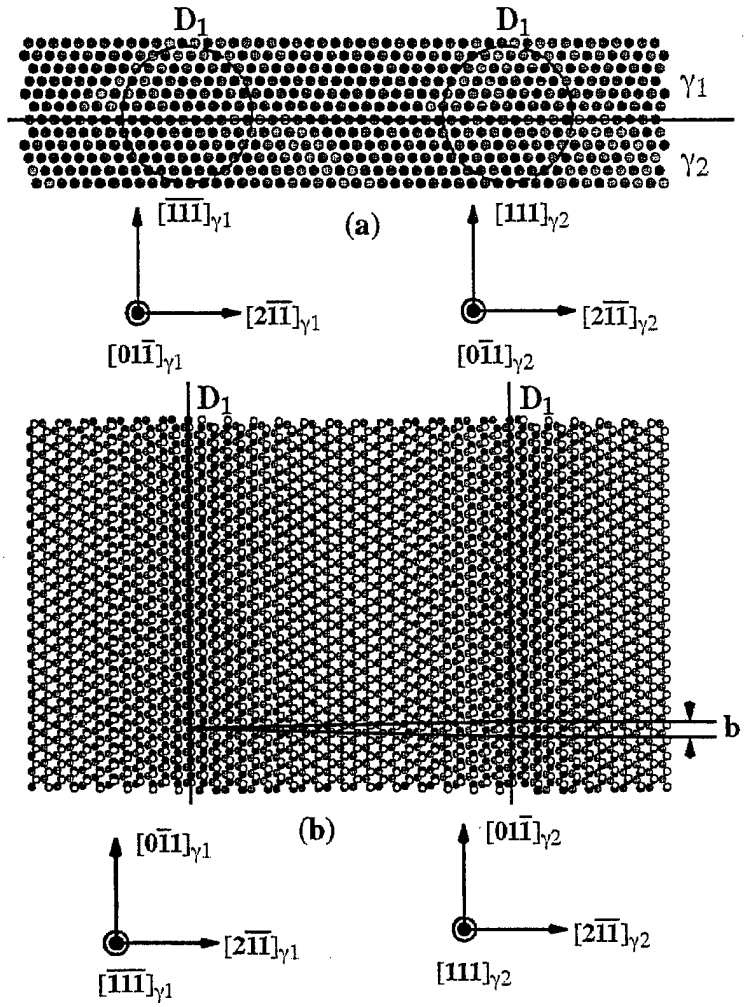

Figure 10 Equilibrium configuration of the $(\bar{1}\bar{1}\bar{1})_{\gamma 1}/(111)_{\gamma 2}$ interface (bicrystal D): (a) Atomic positions projected onto the $(01\bar{1})_{\gamma 1}/(0\bar{1}1)_{\gamma 2}$ plane; (b) Atomic positions projected onto the $(\bar{1}\bar{1}\bar{1})_{\gamma 1}/(111)_{\gamma 2}$ interface plane. Interfacial screw dislocations are marked as D_1.

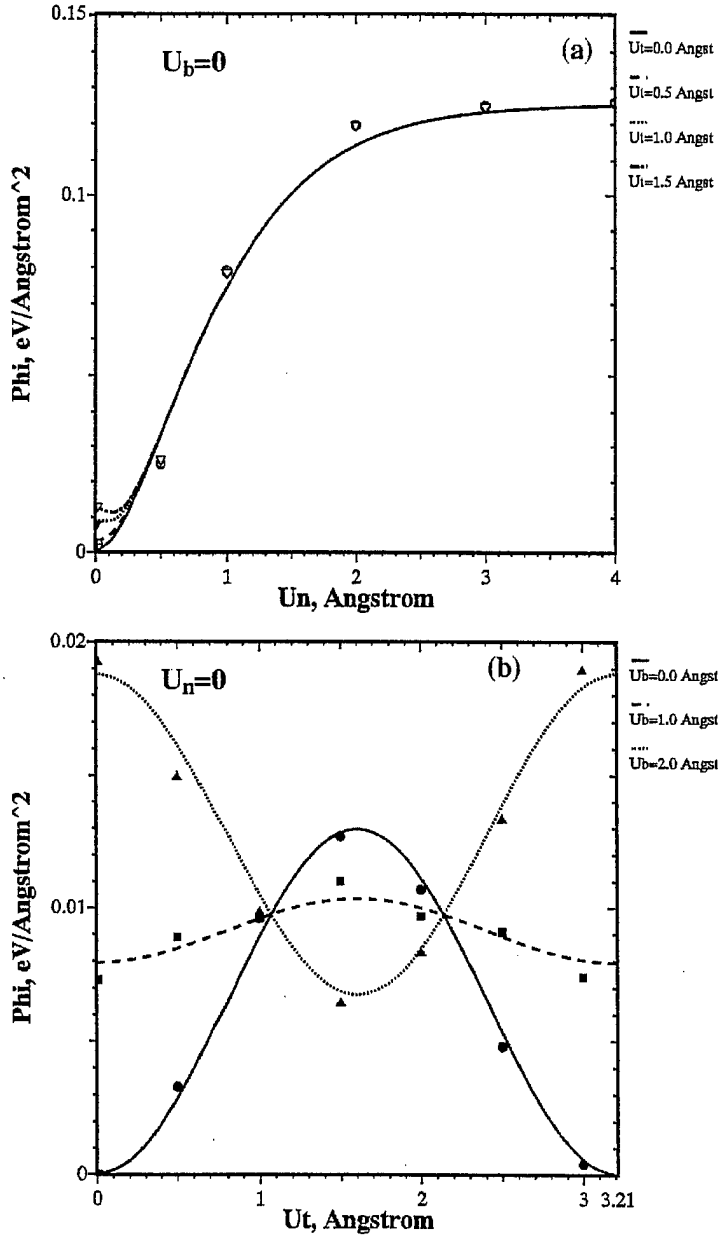

Figure 11 Variation of the decohesion potential for the $(\bar{1}10)_\beta/(111)_\gamma$ interface with the normal displacement U_n in the $[\bar{1}\bar{1}0]_\beta/[\bar{1}\bar{1}\bar{1}]_\gamma$ direction and tangential displacements U_t and U_b in the $[001]_\beta/[0\bar{1}\bar{1}]_\gamma$ and $[1\bar{1}0]_\beta/[2\bar{1}\bar{1}]_\gamma$ directions, respectively.

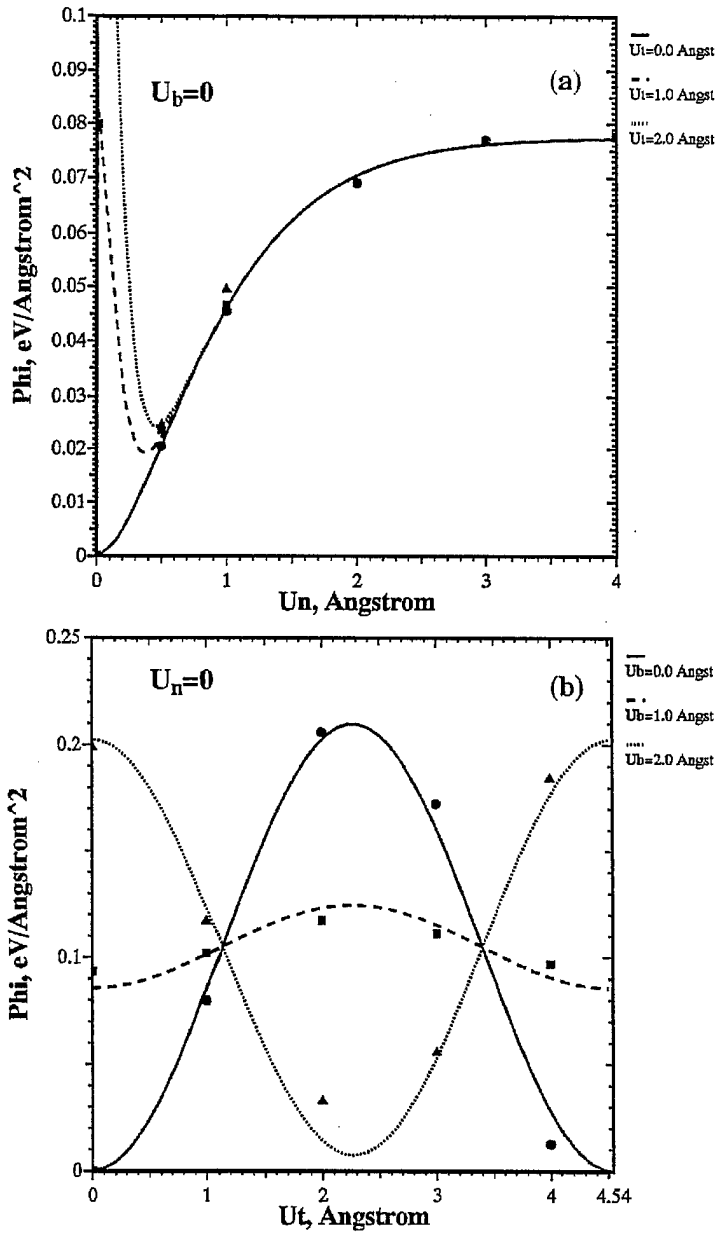

Figure 12 Variation of the decohesion potential for the interface $(001)_\beta/(011)_\gamma$ with the normal displacement U_n in the $[001]_\beta/[0\bar{1}1]_\gamma$ direction and tangential displacements U_t and U_b in the $[\bar{1}\bar{1}0]_\beta/[\bar{1}\bar{1}\bar{1}]_\gamma$ and $[1\bar{1}0]_\beta/[2\bar{1}\bar{1}]_\gamma$ directions, respectively.

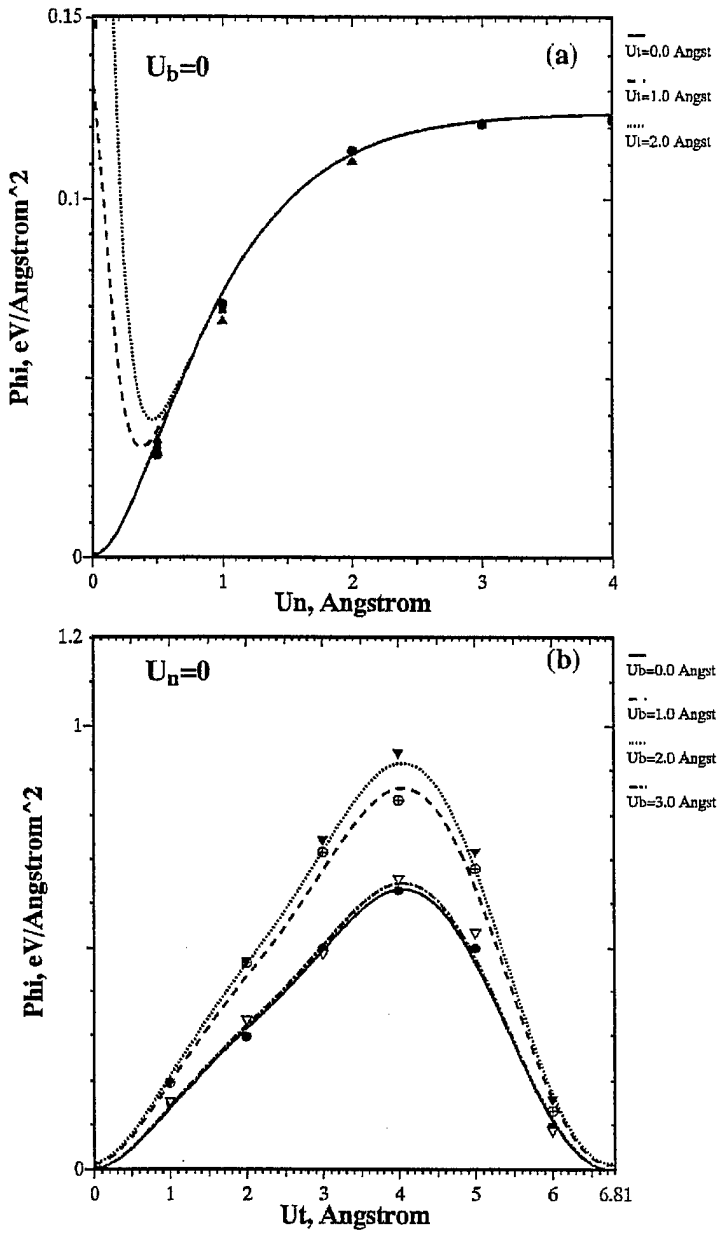

Figure 13 Variation of the decohesion potential for the interface $(110)_\beta/(211)_\gamma$ with the normal displacement U_n in the $[1\bar{1}0]_\beta/[2\bar{1}\bar{1}]_\gamma$ direction and tangential displacements U_t and U_b in the $[\bar{1}\bar{1}0]_\beta/[\bar{1}\bar{1}\bar{1}]_\gamma$ and $[001]_\beta/[0\bar{1}\bar{1}]_\gamma$ directions, respectively.

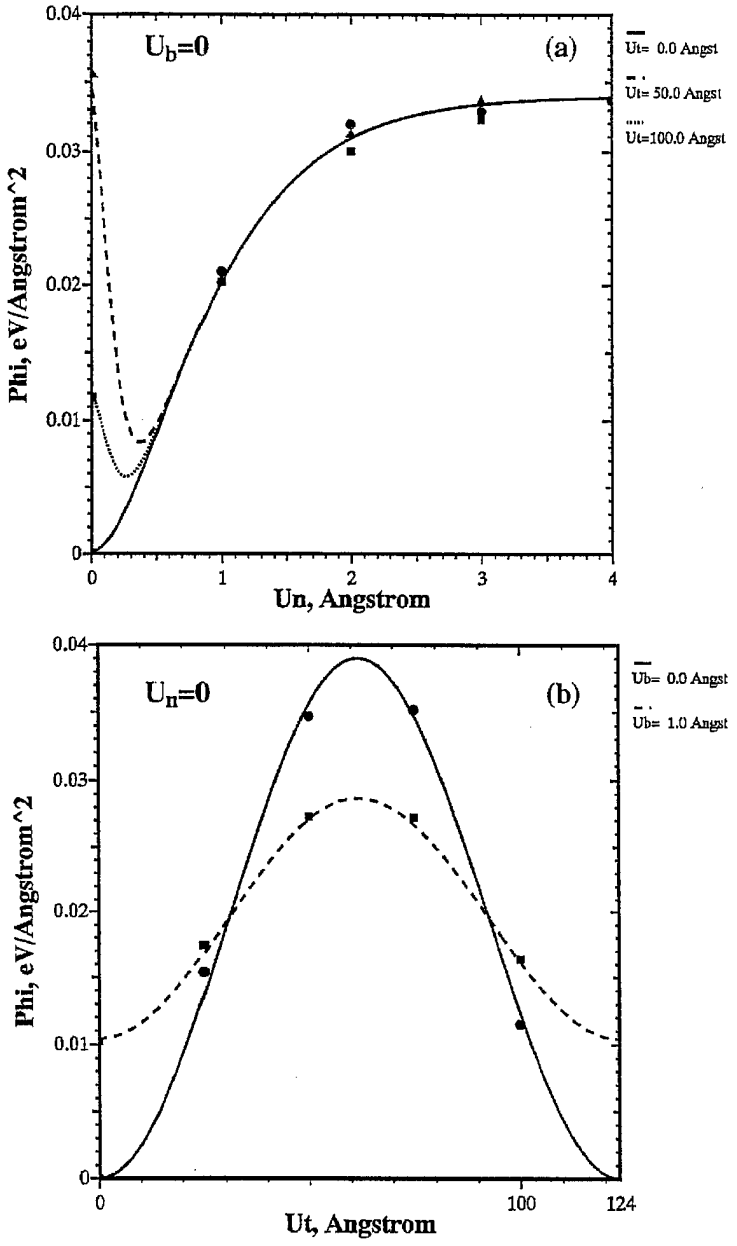

Figure 14 Variation of the decohesion potential for the interface $(\bar{1}11)_{\gamma 1}/(111)_{\gamma 2}$ with the normal displacement U_n in the $[\bar{1}\bar{1}\bar{1}]_{\gamma 1}/[111]_{\gamma 2}$ direction and tangential displacements U_t and U_b in the $[0\bar{1}\bar{1}]_{\gamma 1}/[01\bar{1}]_{\gamma 2}$ and $[2\bar{1}\bar{1}]_{\gamma 1}/[2\bar{1}\bar{1}]_{\gamma 2}$ directions, respectively.

Table I: Parameters Characterizing Interfacial Dislocation for the three Beta/ Gamma and one Gamma/Gamma Interfaces Analyzed in the Present Work

$(\bar{1}\bar{1}0)_\beta/(\bar{1}\bar{1}\bar{1})_\gamma$ Interface: Bicrystal A		
Parameter	**Dislocation Type**	
	D_1	D_2
Line Direction, l	$[1\ \bar{1}\ 0]_\beta$ $[2\ \bar{1}\ \bar{1}]_\gamma$	$[0\ 0\ 1]_\beta$ $[0\ \bar{1}\ 1]_\gamma$
Burger's Vector, b	$1/2\ a_\beta\ [0\ 0\ 1]_\beta$ $1/2\ a_\gamma c_\gamma/\sqrt{a_\gamma^2+c_\gamma^2}\ [0\ \bar{1}\ 1]_\gamma$	$4\ a_\beta/\sqrt{2}\ [\bar{1}\ 1\ 0]_\beta$ $4\ a_\gamma c_\gamma/\sqrt{a_\gamma^2+5c_\gamma^2}\ [2\ 1\ 1]_\gamma$
Dislocation Spacing, λ	$7/2\ a_\beta$ $4\ a_\gamma c_\gamma/\sqrt{a_\gamma^2+c_\gamma^2}$	$10a_\beta/\sqrt{2}$ $14a_\gamma c_\gamma/\sqrt{a_\gamma^2+5c_\gamma^2}$
$(001)_\beta/(0\bar{1}1)_\gamma$ Interface: Bicrystal B		
Parameter	**Dislocation Type**	
	D_1	D_2
Line Direction, l	$[\bar{1}\ \bar{1}\ 0]_\beta$ $[\bar{1}\ \bar{1}\ \bar{1}]_\gamma$	$[\bar{3}\ 4\ 0]_\beta$ $[\bar{3}\ 2\ 2]_\gamma$
Burger's Vector, b	$2\ a_\beta/\sqrt{2}\ [\bar{1}\ 1\ 0]_\beta$ $2\ a_\gamma c_\gamma/\sqrt{a_\gamma^2+5c_\gamma^2}\ [2\ 1\ 1]_\gamma$	$a_\beta/5\ [4\ 3\ 0]_\beta$ $a_\gamma c_\gamma/\sqrt{9a_\gamma^2+25c_\gamma^2}\ [4\ 3\ 3]_\gamma$
Dislocation Spacing, λ	$7\ a_\beta/\sqrt{2}$ $10\ a_\gamma c_\gamma/\sqrt{a_\gamma^2+5c_\gamma^2}$	$21\ a_\beta/5$ $20\ a_\gamma c_\gamma/\sqrt{9a_\gamma^2+25c_\gamma^2}$
$(1\bar{1}0)_\beta/(2\bar{1}\bar{1})_\gamma$ Interface: Bicrystal C		
Parameter	**Dislocation Type**	
	D_1	D_2
Line Direction, l	$[\bar{1}\ \bar{1}\ 0]_\beta$ $[\bar{1}\ 1\ \bar{1}]_\gamma$	$[3\ 3\ 7]_\beta$ $[\bar{1}\ 1\ \bar{3}]_\gamma$
Burger's Vector, b	$1/2\ a_\beta\ [0\ 0\ 1]_\beta$ $1/2\ a_\gamma c_\gamma/\sqrt{a_\gamma^2+c_\gamma^2}\ [0\ \bar{1}\ 1]_\gamma$	$a_\beta/\sqrt{134}\ [\bar{7}\ \bar{7}\ 6]_\beta$ $a_\gamma c_\gamma/\sqrt{a_\gamma^2+65c_\gamma^2}\ [471]_\gamma$
Dislocation Spacing, λ	$7/2\ a_\beta$ $4\ a_\gamma c_\gamma/\sqrt{a_\gamma^2+c_\gamma^2}$	$21\ a_\beta/\sqrt{134}$ $22\ a_\gamma c_\gamma/\sqrt{a_\gamma^2+65c_\gamma^2}$
$(1\bar{1}0)_\beta/(2\bar{1}\bar{1})_\gamma$ Interface: Bicrystal D		
Parameter	**Dislocation Type**	
	D_1	
Line Direction, l	$[0\ \bar{1}\ 1]_\gamma$	
Burger's Vector, b	$1/2\ a_\gamma c_\gamma/\sqrt{a_\gamma^2+c_\gamma^2}\ [0\ \bar{1}\ 1]_\gamma$	
Dislocation Spacing, λ	$25/2\ a_\gamma\sqrt{(a_\gamma^2+2c_\gamma^2)/(a_\gamma^2+c_\gamma^2)}$	

Table II. Decohesion Potential Parameters for the Three Beta/Gamma and One Gamma/Gamma Interface Analyzed in the Present Work

Parameter	Interface Type			
	$(110)_\beta/(111)_\gamma$	$(001)_\beta/(011)_\gamma$	$(110)_\beta/(211)_\gamma$	$(111)_{\gamma 1}/(111)_{\gamma 2}$
Designation	A	B	C	D
n–direction	$[\bar{1}10]_\beta/[\bar{1}\bar{1}\bar{1}]_\gamma$	$[001]_\beta/[0\bar{1}1]_\gamma$	$[1\bar{1}0]_\beta/[2\bar{1}\bar{1}]_\gamma$	$[\bar{1}\bar{1}\bar{1}]_{\gamma 1}/[111]_{\gamma 2}$
t–direction	$[001]_\beta/[0\bar{1}1]_\gamma$	$[\bar{1}\bar{1}0]_\beta/[\bar{1}\bar{1}\bar{1}]_\gamma$	$[\bar{1}\bar{1}0]_\beta/[\bar{1}\bar{1}\bar{1}]_\gamma$	$[0\bar{1}\bar{1}]_{\gamma 1}/[01\bar{1}]_{\gamma 2}$
b–direction	$[1\bar{1}0]_\beta/[2\bar{1}\bar{1}]_\gamma$	$[1\bar{1}0]_\beta/[2\bar{1}\bar{1}]_\gamma$	$[001]_\beta/[0\bar{1}1]_\gamma$	$[2\bar{1}\bar{1}]_{\gamma 1}/[2\bar{1}\bar{1}]_{\gamma 2}$
δ_n, Å	0.5	0.5	0.5	0.5
λ_t, Å	3.21	4.54	6.81	123.5
λ_b, Å	4.54	4.54	3.21	5.78
α_0	–0.013	–0.21	–0.148	–0.039
α_1	–1.5	–1	0.42	–1
α_2	0	0	–0.2	0
α_3	0	0	–3.42	0
α_4	0.5	0	1.17	0
α_5	0	0	–5	0
σ_{max}, GPa	7.37	4.57	7.29	2.01
$\tau_{max,t}$, GPa	1.09	11.77	29.2	0.160
$\tau_{max,b}$, GPa	1.11	5.60	1.20	1.65
$\Phi(U_n \to \infty)$, J/m^2	2.02	1.25	2.03	0.561

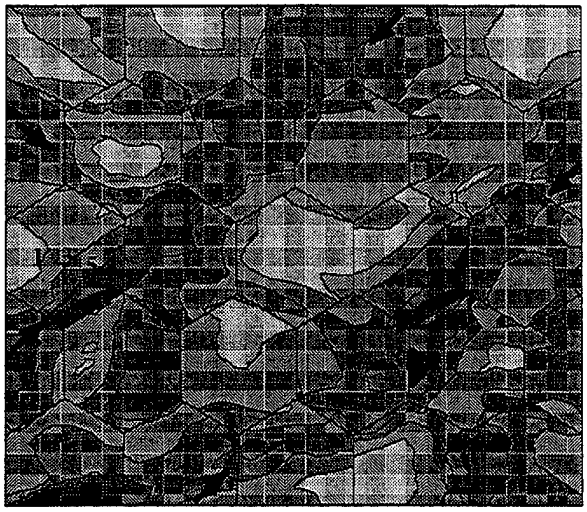

(a)

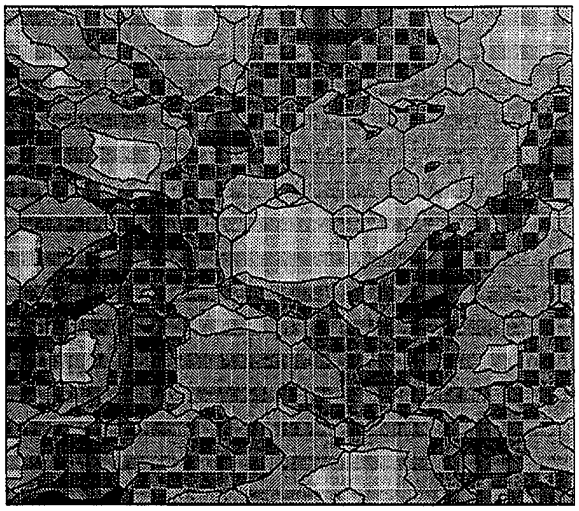

(d)

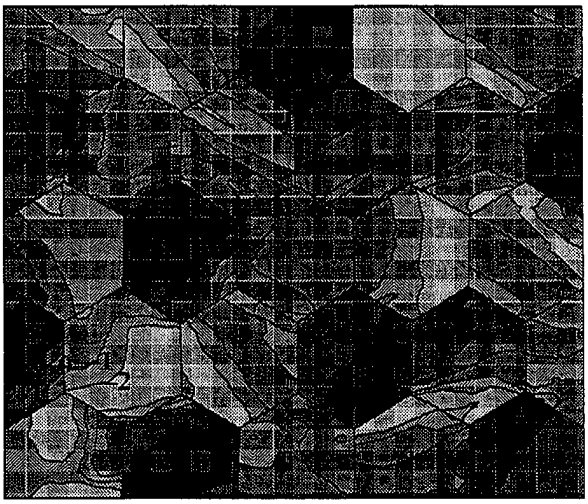

(b)

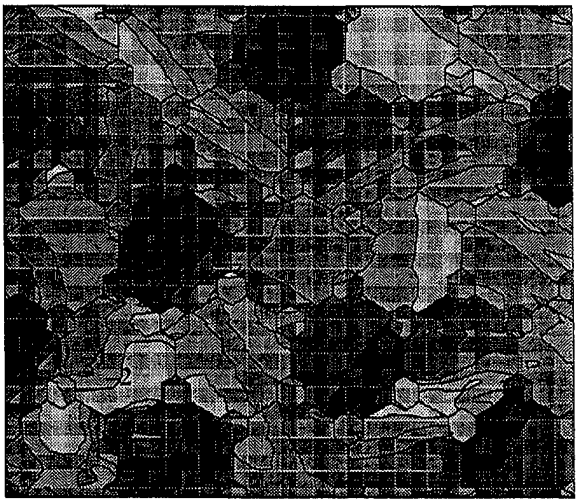

(e)

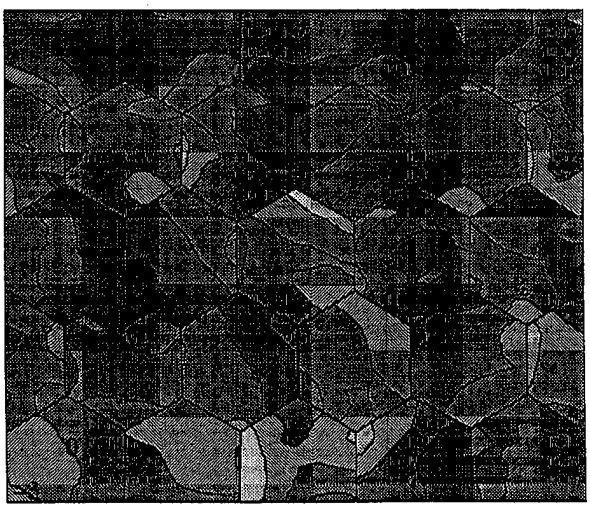

(c)

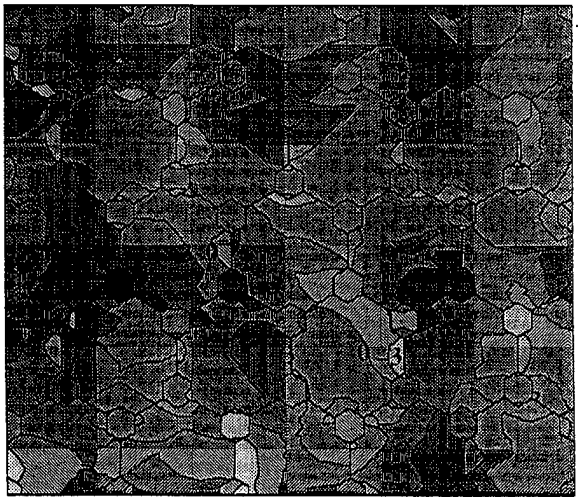

(f)

Figure 9 Contour plots at the overall normal strain of 2% in the vertical direction of: (a) the normal equivalent plastic strain (in percents), (b) the changes in Euler angle (in degrees) and (c) the hydrostatic stress (in 100MPa) for the single–phase (matrix) polycrystalline material in which the grain boundaries are represented using the cohesive zone model, and (d), (e) and (f) are the corresponding contour plots for the two–phase (matrix + stable beta) material.

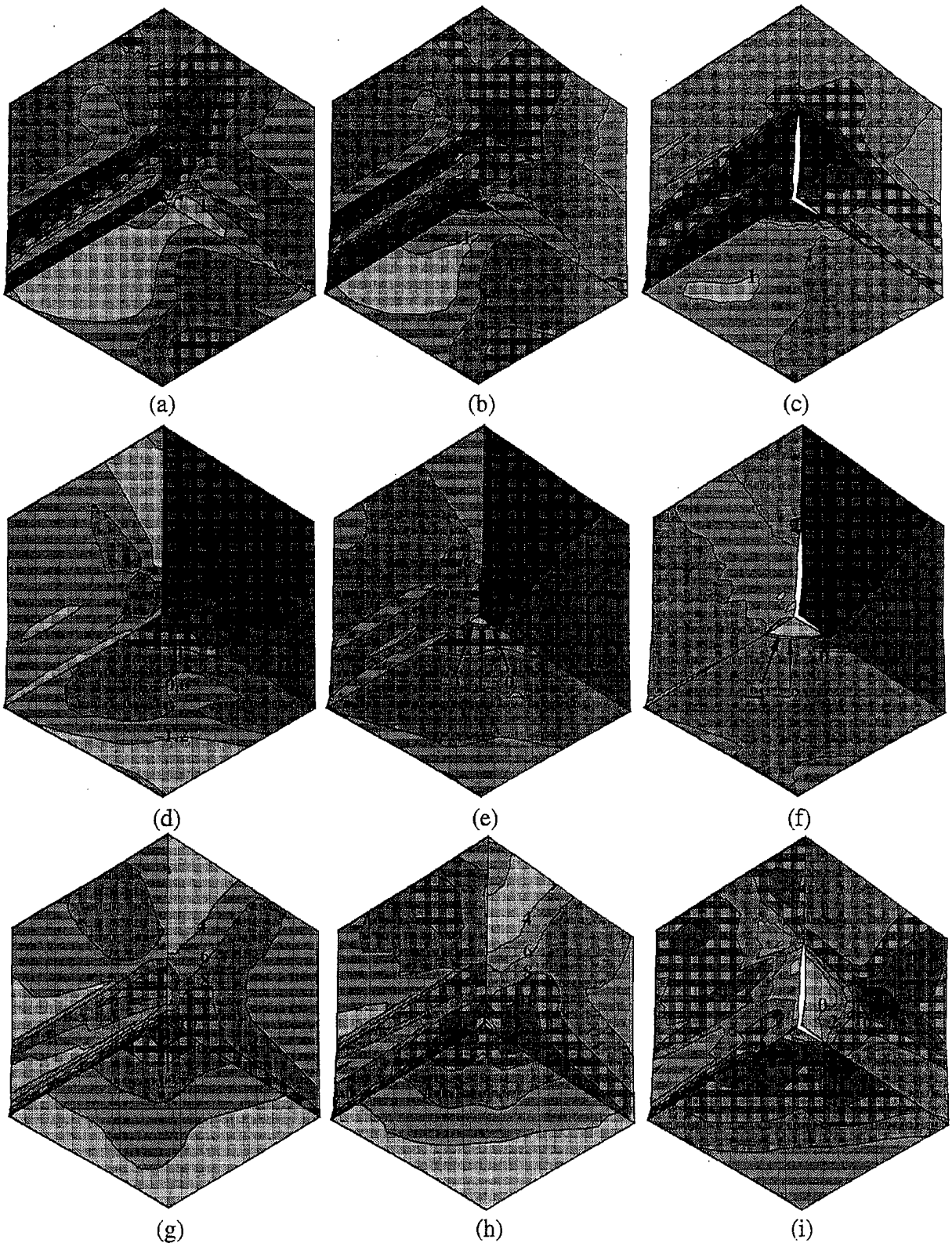
(a)
(b)
(c)
(d)
(e)
(f)
(g)
(h)
(i)

Figure 10 Contour plots for the normal equivalent plastic strain (in percents) for the single–phase (matrix) material at the overall normal strains of (a) 1%, (b) 1.7% and (c) 2.1%. The corresponding contour plots for the change in Euler angle (in degrees) (d), (e) and (f). The corresponding contour plots for the hydrostatic stress (in 100MPa), (g), (h) and (i).

Appendix B

Voronoi Cell Finite Element Analysis

Of

Effective Properties of Functionally Graded Materials

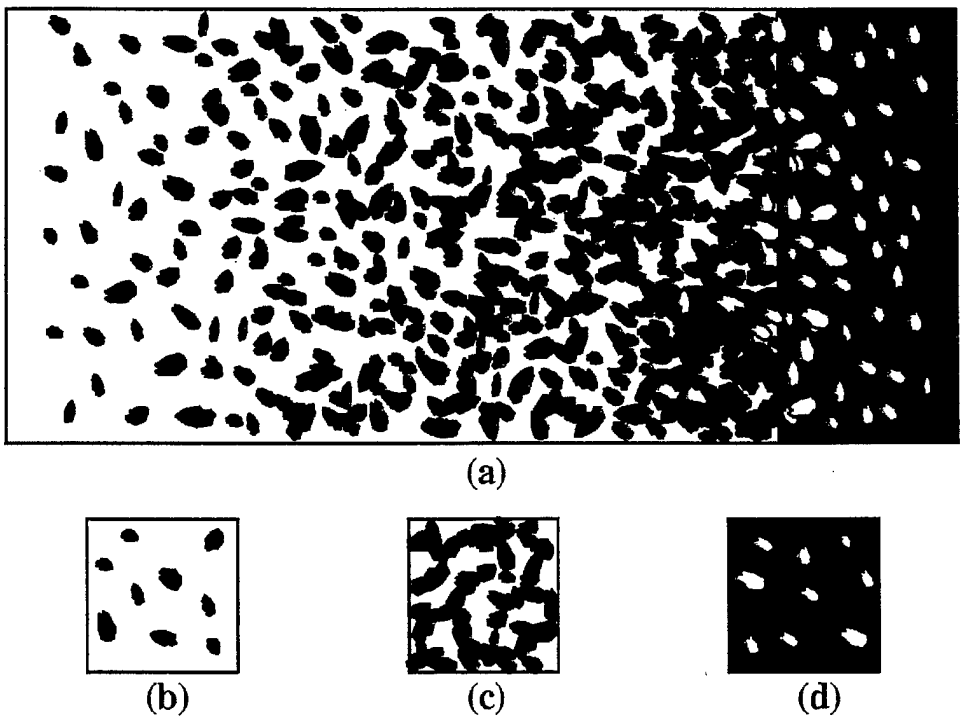

Figure 5. (a) Schematic representation of the microstructure of a graded ceramic/ metal region. The microstructure consisting of dispersed particles embedded in a continuous matrix is observed for large and small volume fractions of the metal and ceramic, as in (b) and (d). In the intermediate region where the volume fractions of the two materials are comparable to each other, the microstructure consists of intertwined clusters of the two phases.

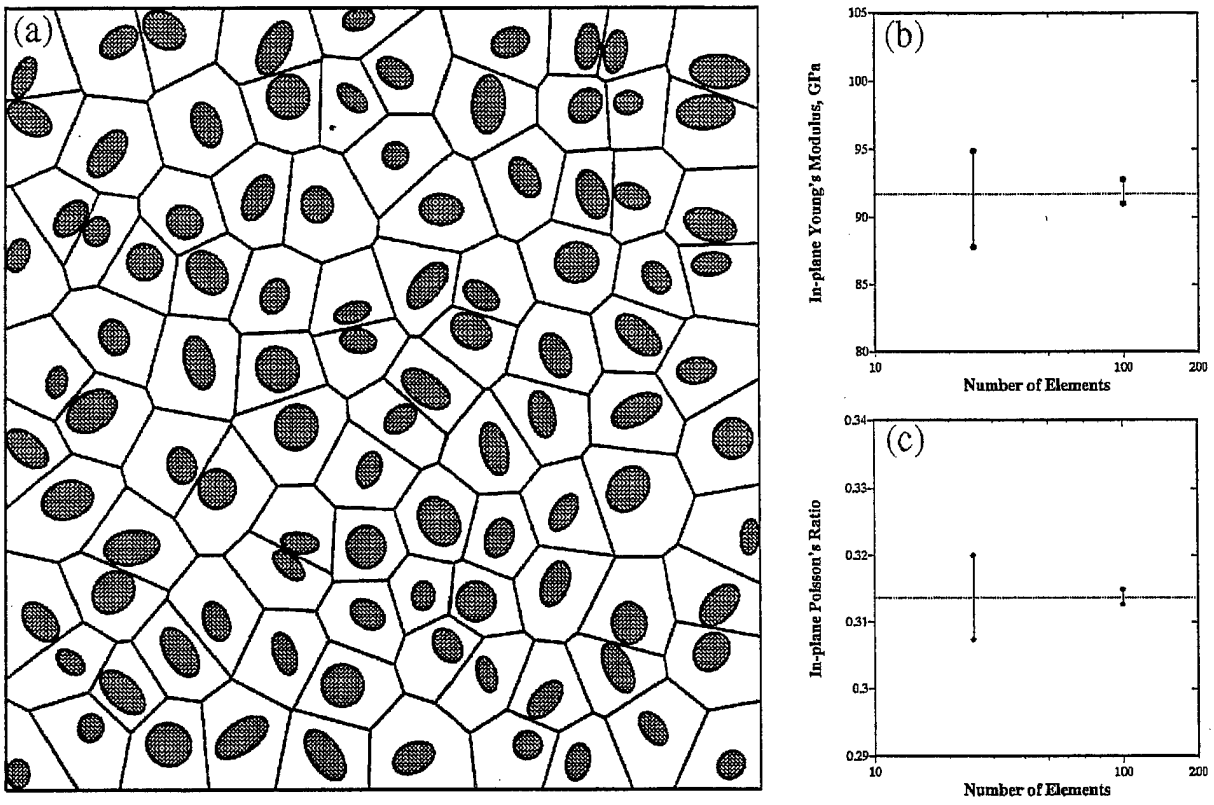

Figure 8. Effect of the number of Voronoi cell elements on the range of in–plane properties for the microstructure consisting of 0.2 volume fraction of elliptical inclusions (aspect ratio in the range 1–2). One of the 100 element square RMEs used is shown in (a), while one of the 25 element square RMEs used is shown in Figures 5(a) and 5(b).

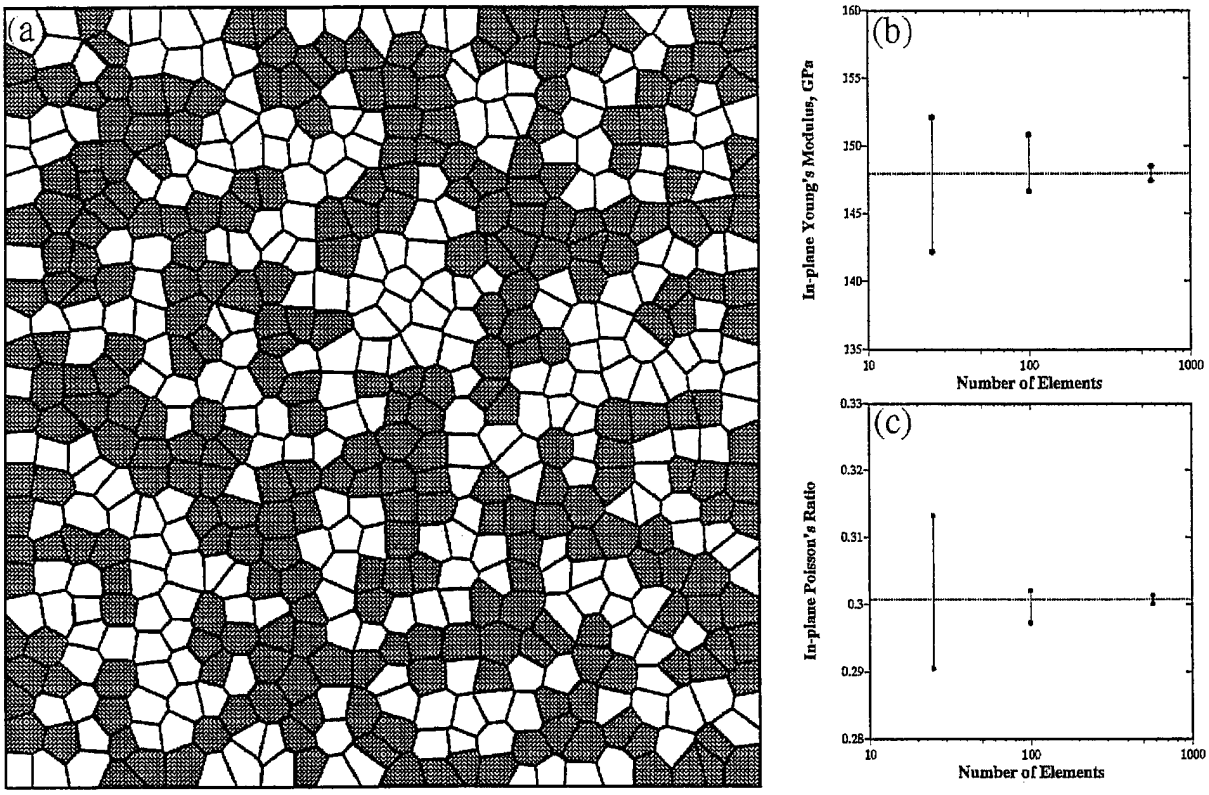

Figure 9. Effect of the number of Voronoi cell elements on the range of in–plane properties for the microstructure consisting of intertwined clusters of the two materials (volume fraction of the two materials ≈ 0.5). One of the 600 element RMEs used is shown in (a).

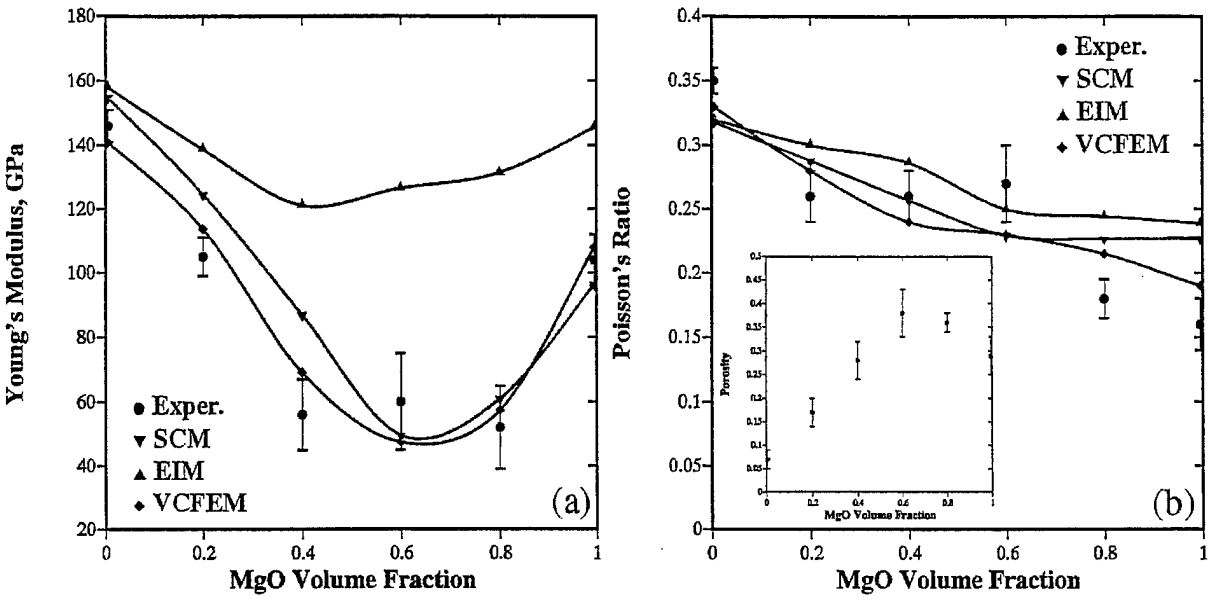

Figure 10. Comparison of the experimentally measured Young's modulus (a) and Poisson's ratio (b) in Ni/MgO FGM with the ones predicted by the Self Consistent Method (SCM), the Equivalent Inclusion Method (EIM) and the Voronoi Cell Finite Element Method (VCFEM). The experimentally measured porosities are shown in the insert of figure (b).

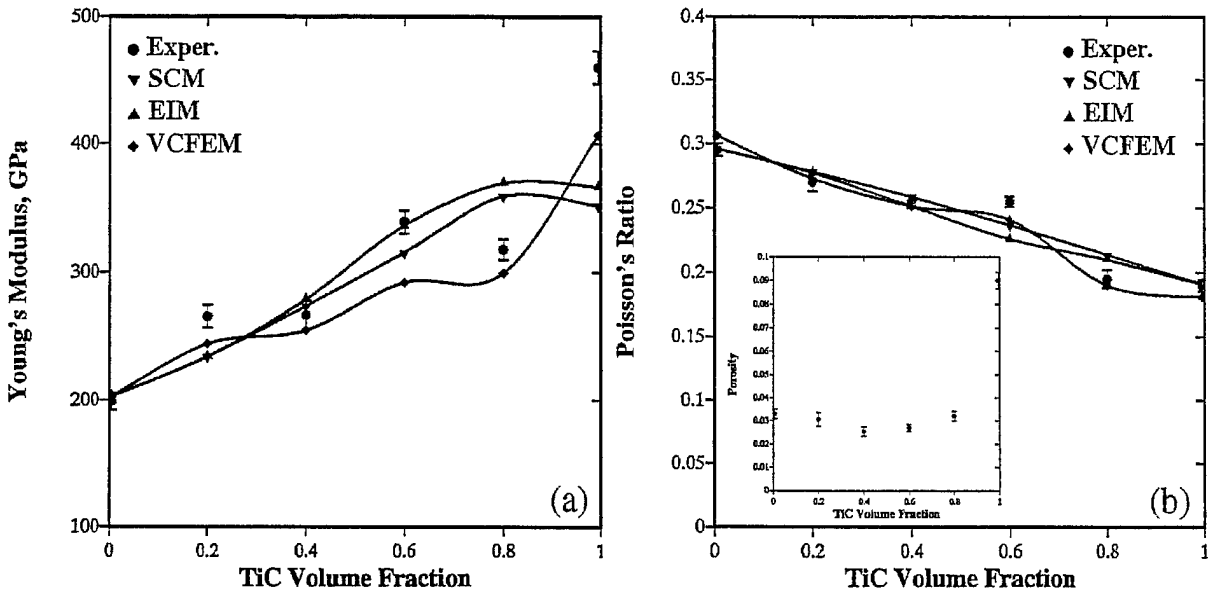

Figure 11. Comparison of the experimentally measured Young's modulus (a) and Poisson's ratio (b) in Ni_3Al/TiC FGM with the ones predicted by the Self Consistent Method (SCM), the Equivalent Inclusion Method (EIM) and the Voronoi Cell Finite Element Method (VCFEM). The experimentally measured porosities are shown in the insert of figure (b).

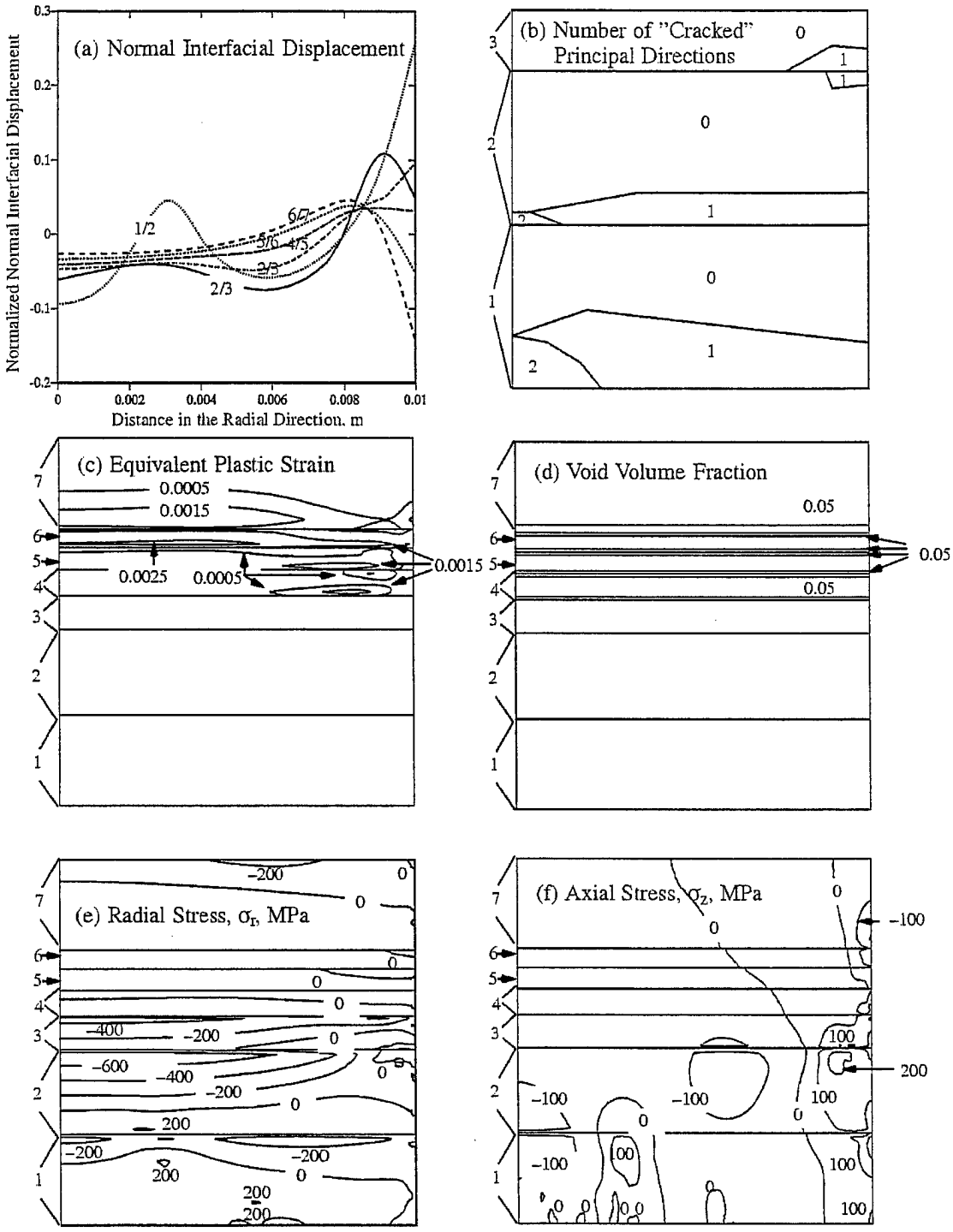

Figure 10. The finite element simulation results of thermally induced: (a) interface decohesion, (b) cracks in Al_2O_3 (layer 1), 90%Al_2O_3/10% 316 stainless steel (layer 2) and 70%Al_2O_3/30% 316 stainless steel (layer 3), (c) plastic strain and (d) voids in 316 stainless steel, (e) radial residual stress, σ_r, and (f) axial residual stress, σ_z, in the case of the graded 316 stainless steel/Al_2O_3 interface characterized by the exponent p=2.0. 1/2, 2/3, etc. in (a) refer to the interfaces separating layers 1 and 2, 2 and 3, etc.

Appendix C

Multiple Asymptotic Solutions For Mixed Mode Fracture In Power Law Hardening Materials

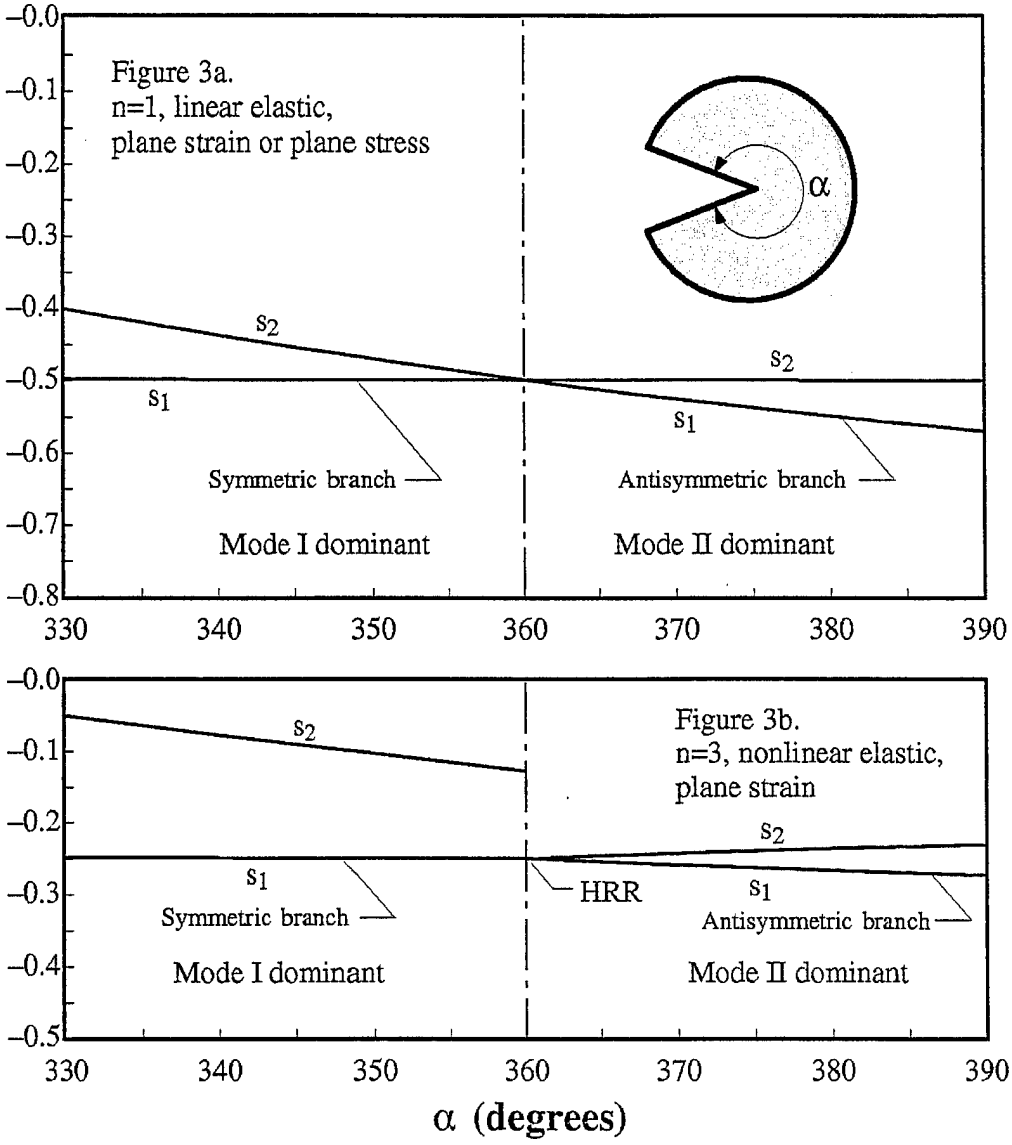

This figure shows how the linear elastic double root for plane strain fracture in the upper figure ($\alpha = 360^\circ, s_1 = s_2 = -0.5$) splits into two distinct asymptotic solutions when material hardening is taken into account in the lower figure. The values of s_1 and s_2 are defined by, $\sigma_{ij}(r,\theta) = A_1 r^{s_1} \overline{\sigma}_{ij}^{1}(\theta) + A_2 r^{s_2} \overline{\sigma}_{ij}^{2}(\theta)$. The mode I dominant solution is higher order ($s_2 > s_1$), while the mode II dominant solution is mixed mode ($s_2 = s_1$).

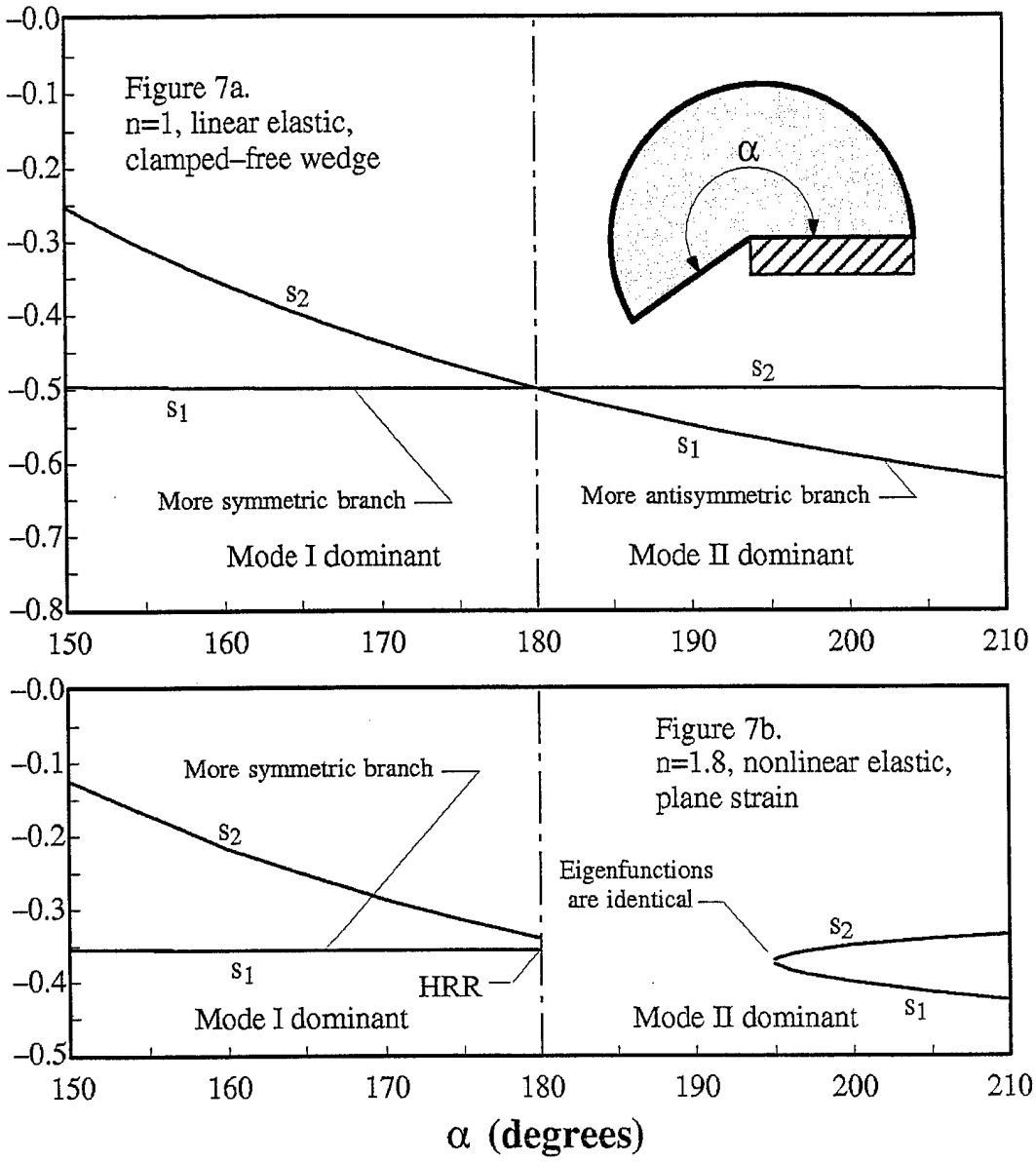

This figure shows how the linear elastic double root for plane strain interface fracture in the upper figure ($\alpha = 180^{\circ}, s_1 = s_2 = -0.5$) splits into two distinct asymptotic solutions when material hardening is taken into account in the lower figure. The values of s_1 and s_2 are defined by, $\sigma_{ij}(r,\theta) = A_1 r^{s_1} \overline{\sigma}^1_{ij}(\theta) + A_2 r^{s_2} \overline{\sigma}^2_{ij}(\theta)$. The mode I dominant solution is higher order ($s_2 > s_1$), while the mode II dominant solution is believed to be non-separable.

Appendix D

Multi-length Scale Modeling
Of
Chemical Vapor Deposition Process

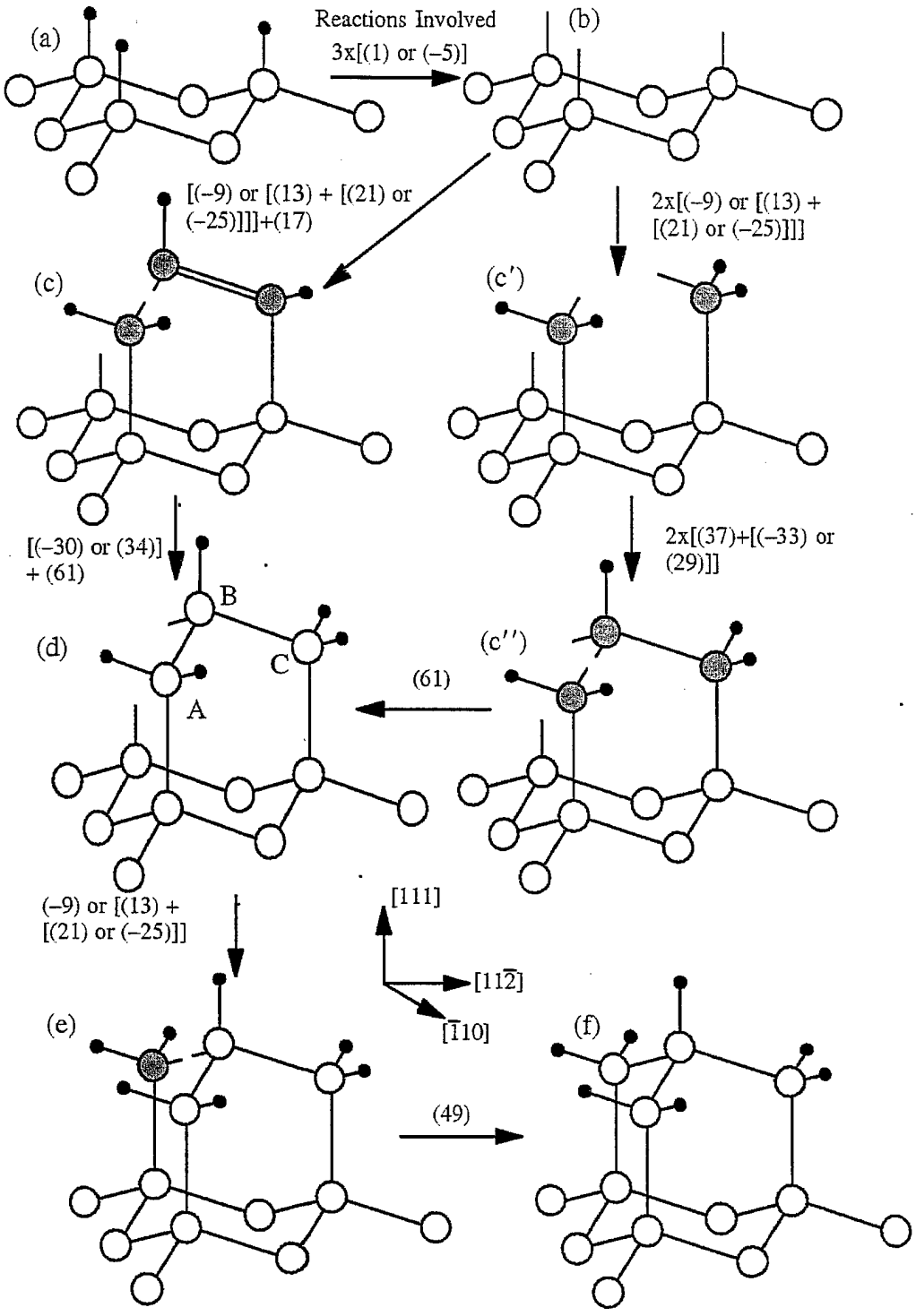

Figure 2. Sequence of steps involved in the nucleation of a new layer on an atomically flat (111) surface. Open circles represent diamond carbon atoms, shaded circles designate hydrocarbon carbon atoms, and small black circles stand for hydrogen atoms. Surface reactions (listed in Table I) involved in various steps of the process are given in parenthesis.

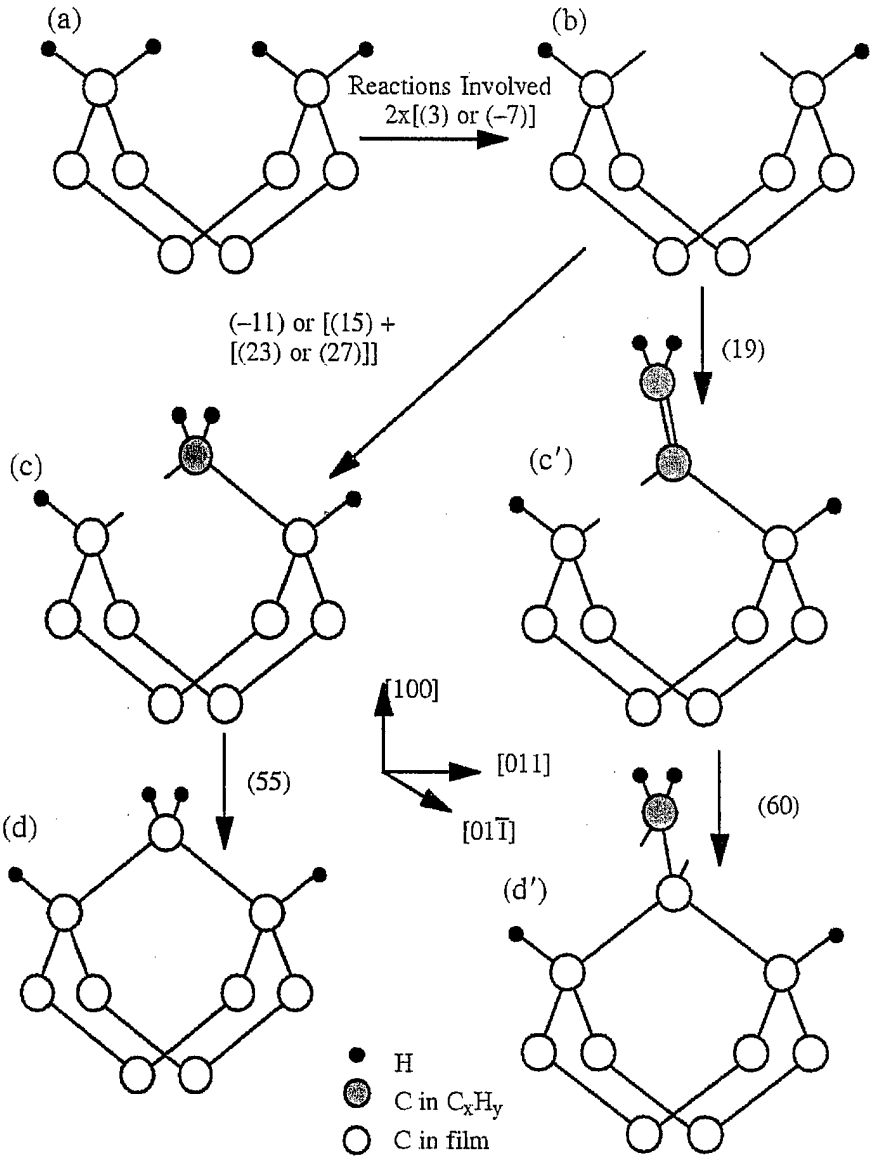

Figure 3. Growth of an (100)–oriented film by trough insertion mechanism. Open circles represent diamond carbon atoms, shaded circles designate hydrocarbon carbon atoms, and small black circles stand for hydrogen atoms. Surface reactions (listed in Table I) involved in various steps of the process are given in parenthesis.

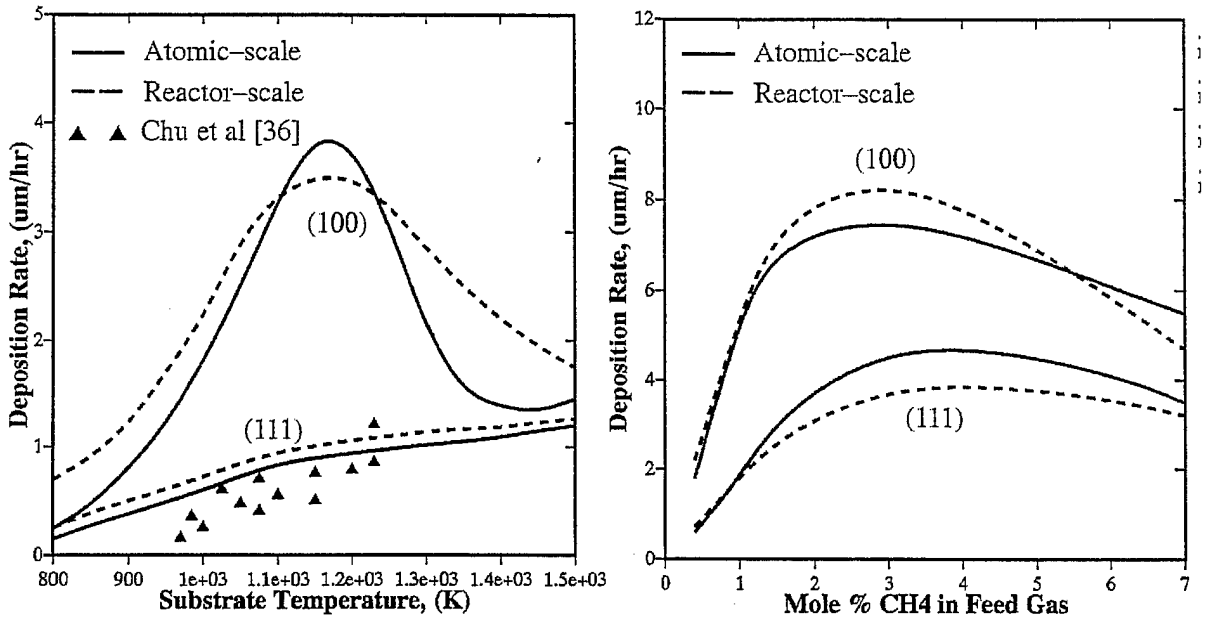

Figure 5. Reactor– and atomic scale analyses predicted (111)– and (100)–oriented film deposition rates as a function of (a) the substrate temperature and (b) concentration of CH_4 in feed gas. The remaining processing condition are as indicated in Figure 4.

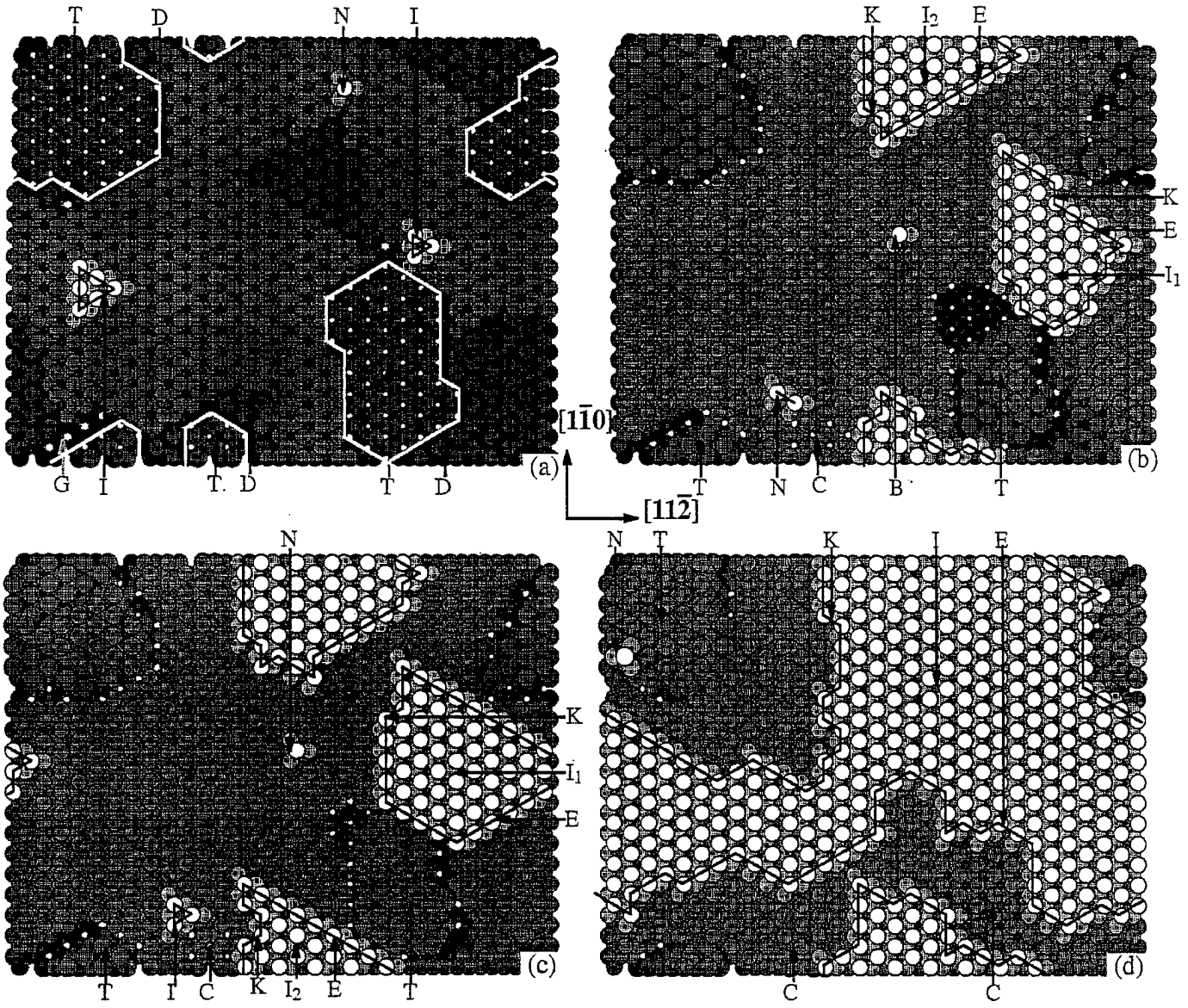

Figure 5. Top view of an (111)–oriented diamond film obtained under the following CVD conditions in the reactor: Reactive gas at the reactor inlet (0.4% CH_4, 92.5% H_2), T_{heator}= 2000 K, $T_{substrate}$= 1000 K, p= 20.25 Torr, Heater–to–Substrate Distance = 1.3cm. Deposition times: (a) 0.87s; (b) 1.81s; (c) 2.07s and (d) 2.85s. Nomenclature: B – 3–carbon bridge, C – Twin covered by regular crystal, D – Dislocation loop, E – Edge, G – Gap, I – Island, K – Kink, N – Nucleus, T – Twin, V – Void

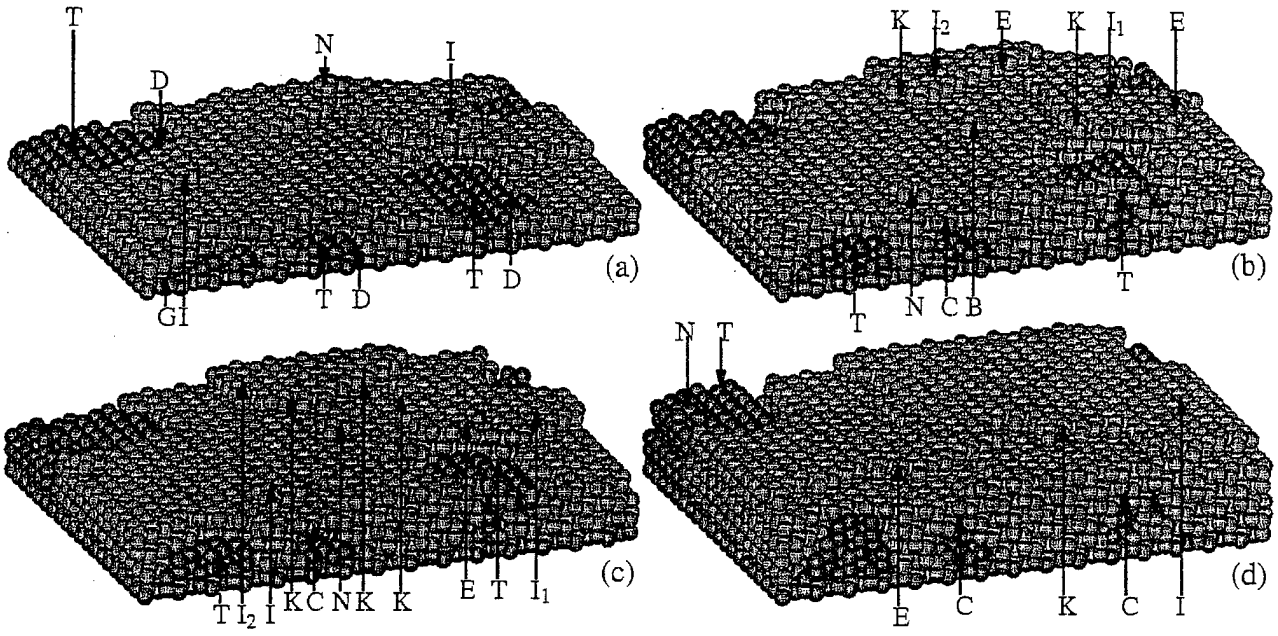

Figure 6. The side view of the four (111)–oriented diamond films shown in Figures 5(a)–(d).

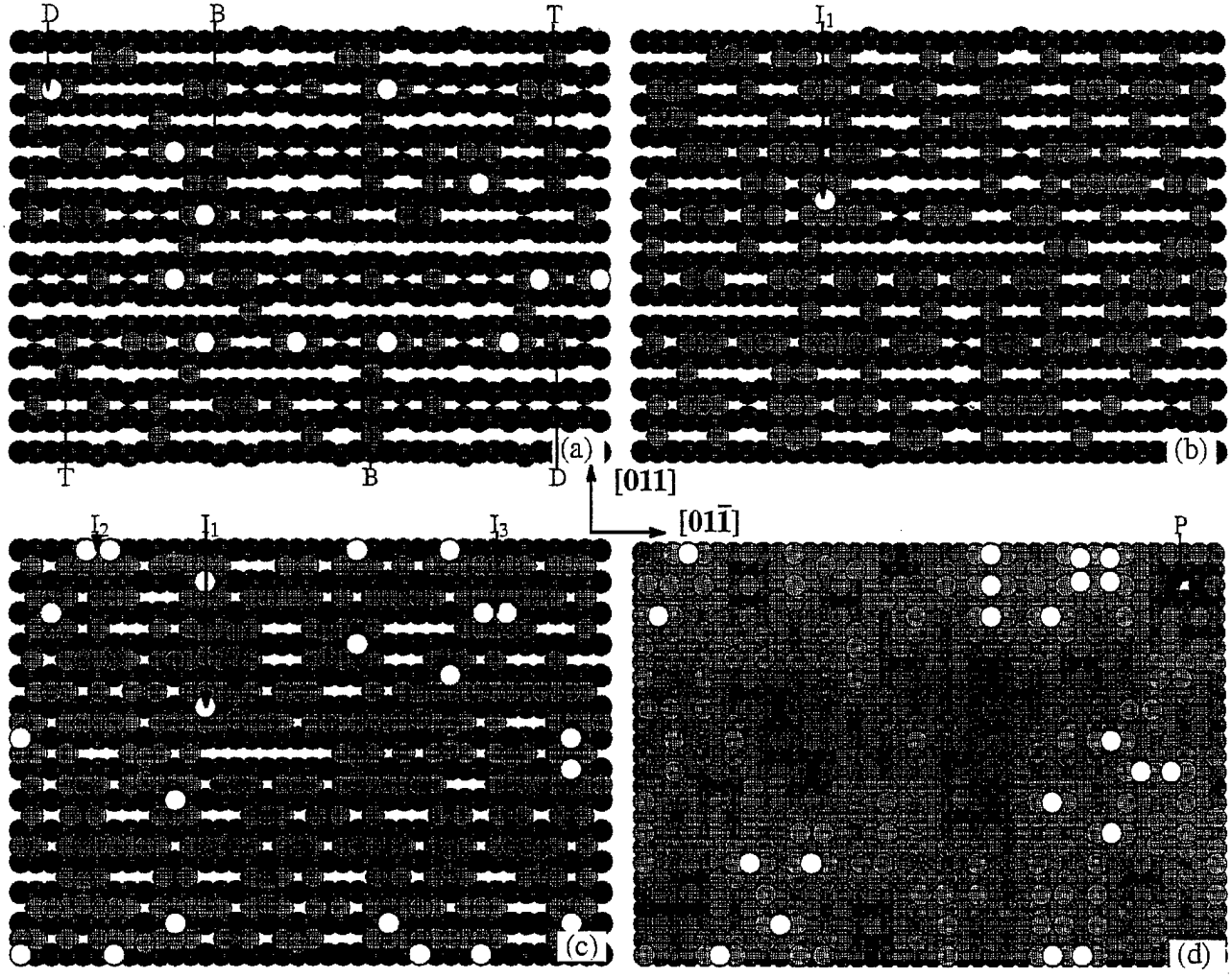

Figure 9. Top view of four (100) surface configurations obtained under the CVD conditions identical to the ones listed in Figure 5. Deposition times: (a) 0.01s; (b) 0.018s; (c) 0.032s and (d) 0.208s. Nomenclature: B—BCN mechanism, D—Dimer insertion mechanism, P—Pit, I—Island, T—Trough insertion mechanism.

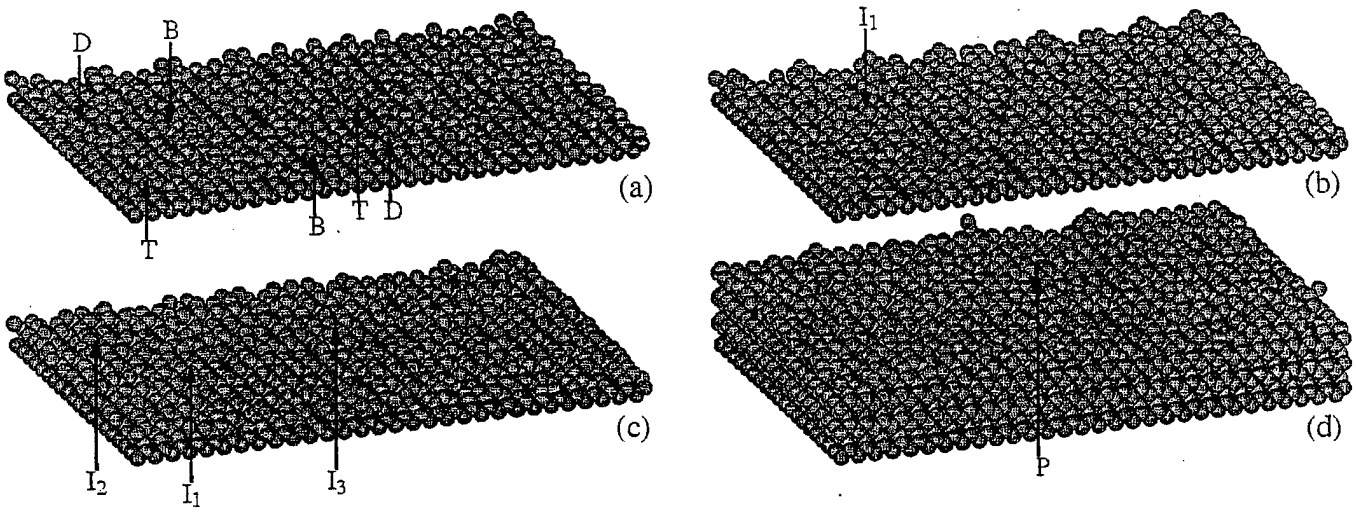

Figure 10. Side view of the four (100)–oriented diamond films shown in Figures 9(a)–(d).

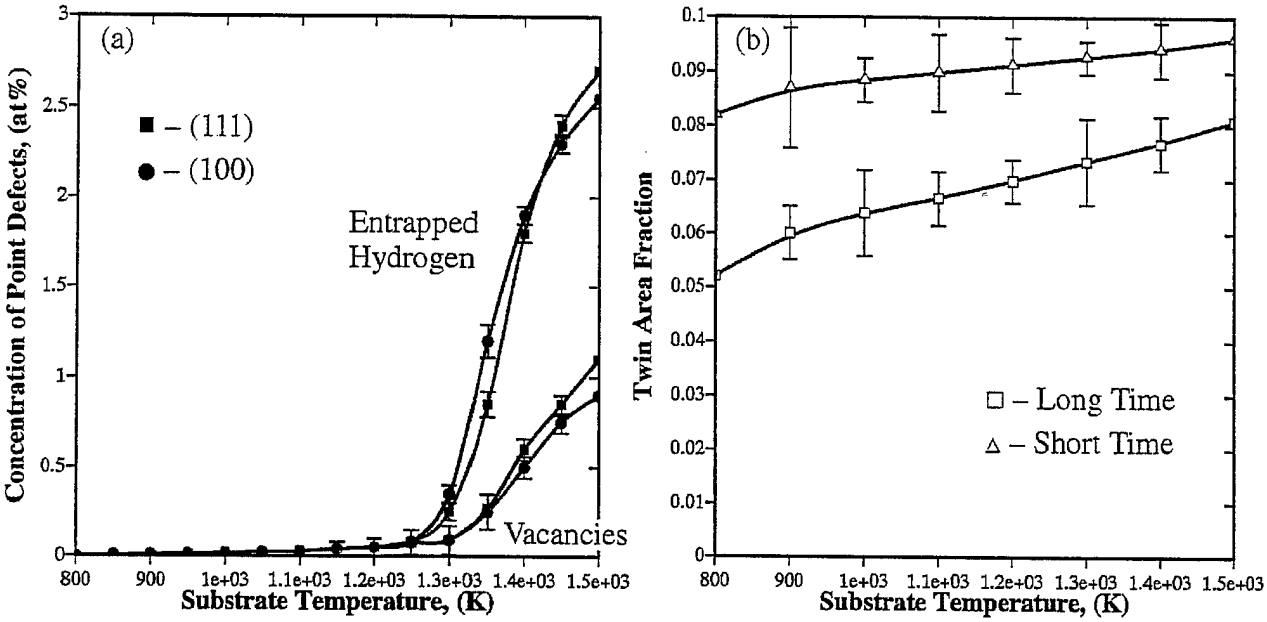

Figure 8. Effect of the substrate temperature on the concentration of vacancies and entrapped hydrogen atoms in (111)– and (100)–oriented diamond films, (a), and twins in (111)–oriented diamond films, (b), under the CVD conditions specified in Figure 5. Error bars represent on standard deviation over five simulation runs.

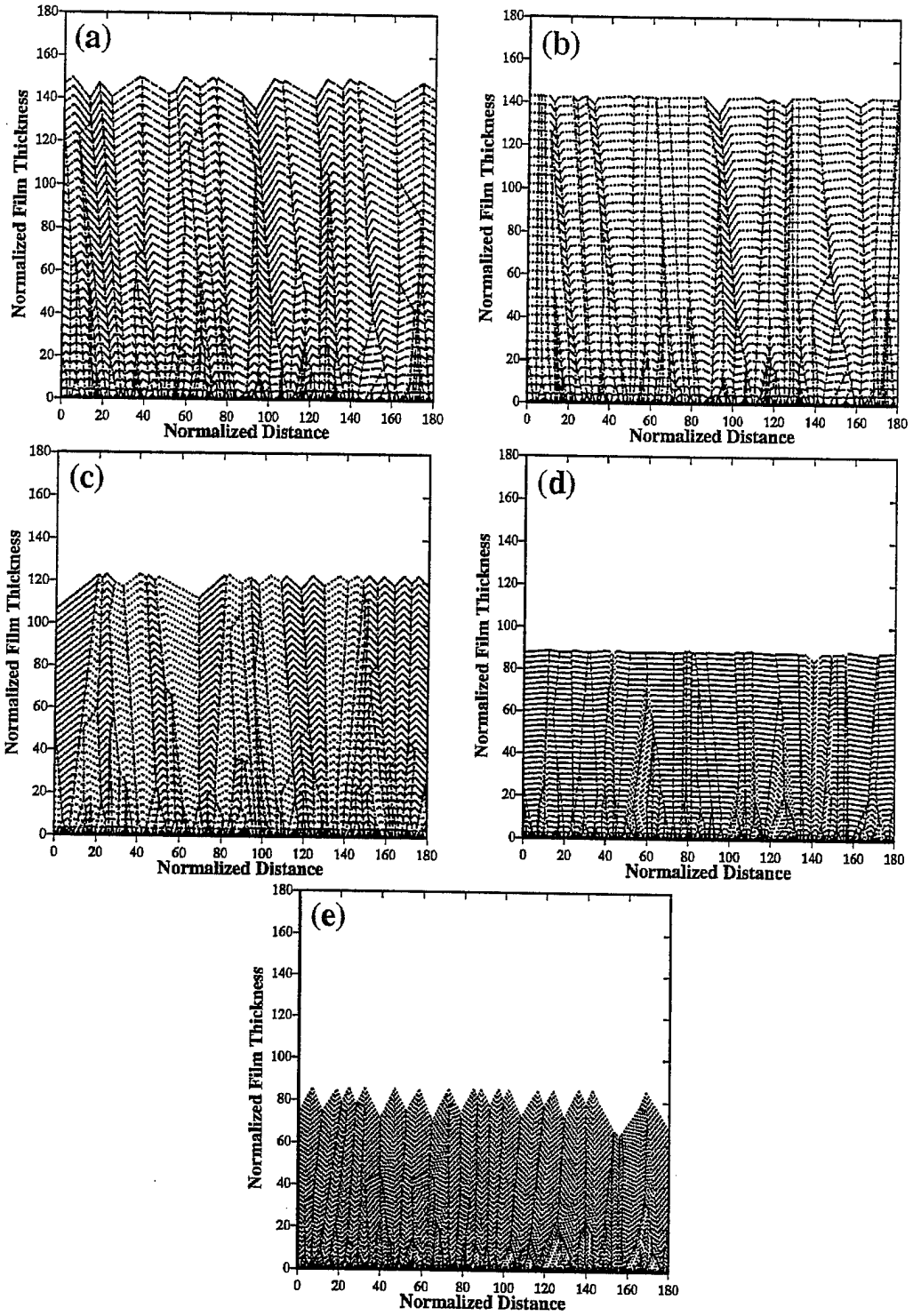

Figure 2. **The microstructure of polycrystalline diamond films deposited under the growth-rate parameter, α=: (a) 1.0; (b) 1.05; (c) 1.5; (d) 2.95 and (e) 3.0. Both the x- and y-axis are normalized with respect to the average nucleus spacing, d_0. The following line type nomenclature is used: dash-dot=grain boundaries, solid={100} facets, dotted ={111} facets, dashed = {100}/{100} facets, and three-dot space={111}/{111} facets.**

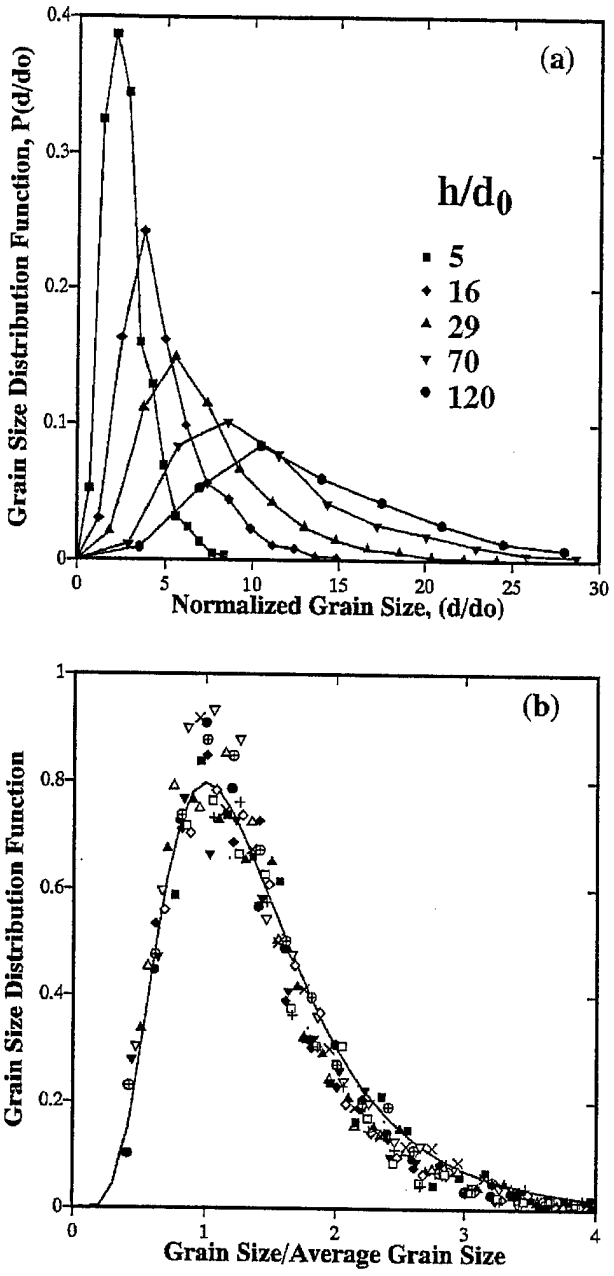

Figure 4. (a) The distribution function for the grain size normalized with respect to the average nucleus spacing, d_0, at five film thicknesses for the growth–rate parameter α=1.5. (b) The distribution function for the grain size normalized with respect to the corresponding average grain size, $\bar{d}$, for five α values and three film thicknesses.

Appendix E

Bernes 2000

Prototype Scale

Chemical Vapor Deposition Reactor

Multi-length Scale Modeling and Processing of FGMs

Technical Monitor: Dr. David M. Stepp

Investigators: R.J. Diefendorf, J.G. Goree, M. Grujicic, P.F. Joseph

Bernex 2000 CVD Reactor

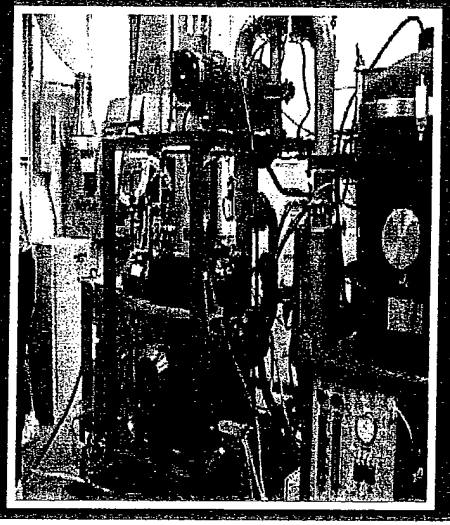

Pumping System

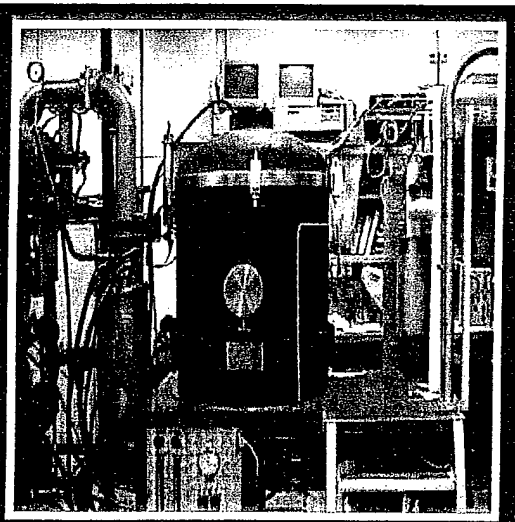

Reactor Furnace

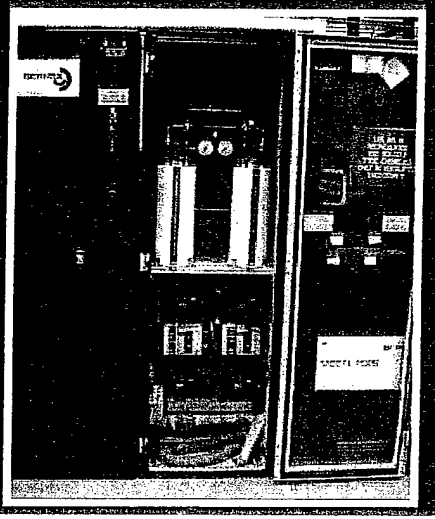

Liquid Precursor Supply System